Effects of the Y432S Cancer-Associated Variant on the Reaction Mechanism of Human DNA Polymerase κ

Yazdan Maghsoud,[1] Arkanil Roy,[1] Emmett M. Leddin,[2] and G. Andrés Cisneros*[,1,3]

[1]*Department of Chemistry and Biochemistry, University of Texas at Dallas, Richardson, TX 75080, USA*

[2]*Department of Chemistry, University of North Texas, Denton, TX 76201, USA*

[3]*Department of Physics, University of Texas at Dallas, Richardson, TX 75080, USA*

**E-mail: andres@utdallas.edu*

ABSTRACT

Human polymerases are vital for genetic information management. Their function involves catalyzing the synthesis of DNA strands with unparalleled accuracy, which ensures the fidelity and stability of the human genomic blueprint. Several disease-associated mutations and their functional impact on DNA polymerases have been reported. One particular polymerase, human DNA polymerase kappa (Pol κ), has been reported to be susceptible to several cancer-associated mutations. The Y432S mutation in Pol κ, which is associated with various cancers, is of interest due to its impact on polymerization activity and markedly reduced thermal stability. Here, we have used computational simulations to investigate the functional consequences of the Y432S by means of classical molecular dynamics (MD) and coupled quantum mechanics/molecular mechanics (QM/MM) methods. Our results suggest that Y432S results in structural effects on domains involved in nucleotide addition and ternary complex stabilization while maintaining catalytic competence. Calculation of the minimum energy path associated with the reaction mechanism of wild type (WT) and Y432S Pol κ indicate that while both enzymes are catalytically competent, the cancer mutation results in a slightly endoergic reaction and an increase in the catalytic barrier. Interactions with a third magnesium ion and environmental effects on non-bonded interactions, particularly involving key residues, contribute to the kinetic and thermodynamic distinctions between the WT and mutant during the catalytic reaction. The energetics and electronic findings suggest that active site residues favor the catalytic reaction with $dCTP^{3-}$ over $dCTP^{4-}$.

1 INTRODUCTION

DNA damage is a constant threat arising from both internal and external agents. DNA adducts, when formed, have the potential to cause mutations that can subsequently lead to diseases and the death of cells.[1] DNA undergoes spontaneous hydrolysis inside the cell, affecting its phosphodiester, N-glycosylic, and amino bonds. Additionally, DNA is under constant attack by oxygen free radicals, which harm the sugar and bases. Sunlight and exposure to chemical pollutants further exacerbate this issue. Even though DNA lesions can be corrected through nucleotide excision repair[2] (NER) and base excision repair[3] (BER) processes, many remain unrepaired. These unrepaired lesions obstruct ongoing transcriptional elongation by RNA polymerases and replication by DNA polymerases.

DNA polymerases are organized into seven families: A, B, C, D, X, Y, and reverse transcriptase (RT).[4] The Y-family polymerases can perform trans-lesion synthesis (TLS), which involves bypassing a damaged DNA site by performing untemplated synthesis.[5, 6] This family is conserved across all life domains, including bacteria, archaea, and eukaryotes, and it plays a crucial role in DNA repair and replication. Under certain conditions, this function may occur when the DNA template is compromised or contains various lesions, such as DNA adducts or thymine dimers resulting from exposure to UV radiation.[7-9]

Y-family polymerases bypass specific lesions with varying accuracies and efficiencies, depending on the type of adduct.[6] DNA polymerase kappa (Pol *κ*) is a part of this family and exhibits differences in nucleotide incorporation specificity and mismatch extension capability when compared to other Y-family polymerases, i.e., Pol *ι*, Pol *η*, and REV1. It demonstrates the highest level of fidelity among the other three members, with a misincorporation rate ranging from ~10^{-3} to 10^{-4} when dealing with all four template bases.[10] However, Pol *κ* effectively extends mispaired primer termini, exhibiting an extension frequency of ~10^{-1} to 10^{-2}.[11] In both *in vitro* settings and within mammalian cells, Pol *κ* exhibits a remarkable capacity for nearly error-free bypass of bulky lesions linked to the amino group of guanine located within the B-DNA minor groove;[12-15] however, it can be inhibited by major groove adducts.[16-19]

Y-family members share common structural elements with replicative DNA polymerases, including the thumb, palm, and fingers domains. The palm domain is where DNA binds during polymerase activity and is also the site for phosphoryl transfer/nucleotide addition. The thumb domain is generally involved in positioning and guiding DNA through the polymerase, while the fingers domain aligns the incoming nucleotide with the template strand and may contribute to recognizing the correct incoming nucleotide.[20] The Y-family also possesses a distinctive fourth domain, referred to as the little finger or polymerase-associated domain (PAD), which engages with the major groove of DNA.[21-25]

Pol *κ* features an additional, unique N-terminal domain known as the N-clasp (**Figure 1A**).[26, 27] This N-clasp domain has been observed to interact with DNA and plays a role in stabilizing the ternary complex formed by the polymerase, DNA, and deoxyribonucleotide triphosphate (dNTP).[28, 29] This is accomplished through interactions involving the catalytic core, the PAD, and the DNA duplex region.[30] Pol *κ* consists of

870 amino acid residues; however, investigations using protein truncations and primer extension assays have revealed that amino acids 19–526 are sufficient to preserve polymerization activity comparable to wild type (WT).[26, 31, 32] Notably, truncated protein versions have demonstrated enhanced stability compared to the full-length protein, making them more prevalent in experimental studies.[31, 33] Conversely, the removal of the N-clasp notably diminishes activity, with implications for lesion bypass, as this domain interacts with the DNA.[34, 35]

Several single nucleotide polymorphisms (SNPs) associated with different cancer phenotypes, resulting in missense mutations on Pol κ, have been reported.[36] Subsequently, some of these cancer-associated SNP variants, along with many others, have been identified in the *POLK* gene, potentially influencing the Pol κ function in various ways.[31] Mutations reducing Pol κ activity can heighten cell sensitivity to DNA-damaging agents, including certain chemotherapeutics. Changes in Pol κ fidelity might influence the genomic stability of tumors. Furthermore, SNP variants in Pol κ with enhanced lesion bypass capability can contribute to resistance against DNA-damaging chemotherapy.[37]

Song et al.[38] and Antczak et al.[39] characterized several cancer-associated variants of Pol κ with similar, lower, or higher activity than the WT protein. Among the studied variants, the Y432S mutant (**Figure 1B**) exhibited considerably lower polymerase activity than the WT, with 20- to 34-fold decreases in k_{cat}/K_m for dCTP insertion opposite G compared to that of WT[38] and significantly reduced thermal stability.[39] Moreover, molecular dynamics (MD) simulations with undamaged DNA revealed that when this variant is paired with the correct incoming nucleotide, it mimicked the behavior of WT with the incorrect incoming nucleotide, suggesting an adoption of an inactive conformation.[39] However, whether this mutation affects the dynamics, the kinetics of the catalytic polymerization reaction, or both, remains elusive. Furthermore, a thorough examination of both proximal and distal effects of enzyme residues on the active site during the pre-catalytic and catalytic stages of the reaction could offer valuable insights into predicting other variants' behavior that have not been discovered thus far.

In the present study, we have investigated the effects of the Y432S variant on the dynamics and kinetics of the polymerization reaction compared to that of WT Pol κ via classical molecular dynamics (MD) and coupled quantum mechanics/molecular mechanics (QM/MM) to study the thermodynamics and kinetics of the reaction between the WT and Y432S with dCTP as the incoming nucleotide. The following sections of the paper outline our approach for MD and QM/MM simulations, encompassing structural, dynamic, and kinetic analyses for both the WT and Y432S systems. Subsequent segments present and discuss the results for each system, exploring their implications in relation to one another. Finally, concluding remarks summarizes the discussion.

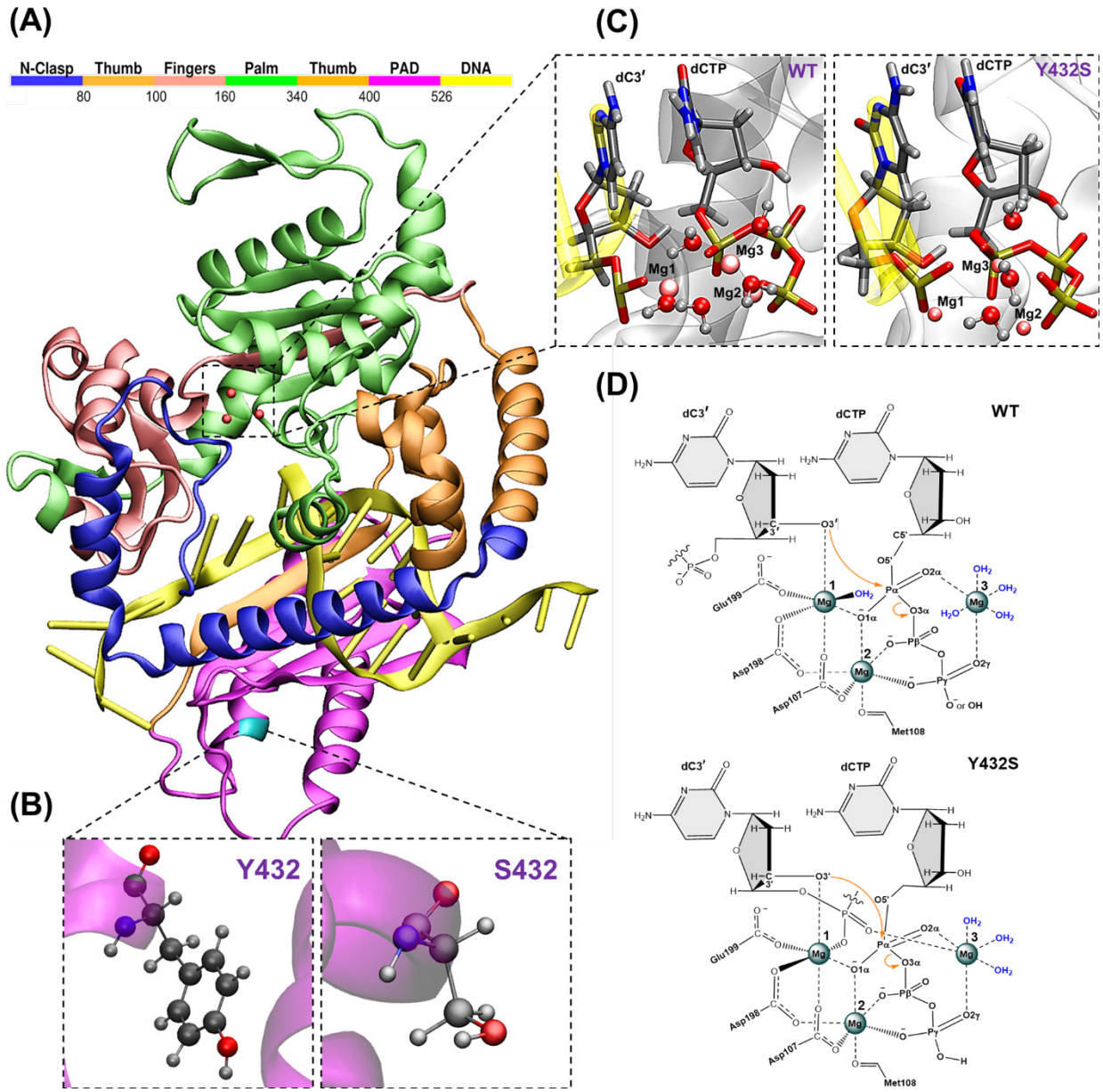

Figure 1. (A) 3D structure of human DNA polymerase κ with three magnesium cations in the active site, modeled from the 2OH2 crystal structure. **(B)** Close-up magnifications illustrating the position of the Y432S mutation. **(C)** 3D close-ups of the active site for WT Pol *κ* and the Y432S variant. **(D)** Stereochemistry of the three-metal active site for the WT and Y432S mutant reactant, along with the proposed S_N2 nucleophilic attack in this study. Orange arrows indicate S_N2 nucleophilic attacks, and coordinated water molecules to the metal centers are labeled in blue. In the WT, one water molecule is coordinated to Mg1, and four are coordinated to Mg3. In the Y432S variant, three water molecules are coordinated to Mg3, while two dC3 phosphodiester bridge oxygens are coordinated to Mg1 and Mg3.

2 COMPUTATIONAL METHODS

2.1 Molecular Dynamics (MD) Simulations

The WT Pol *κ* system was modeled based on a ternary structure of Pol *κ* (PDB ID: 2OH2[30]) bound with the cytidine triphosphate ligand. This specific PDB structure was chosen to maintain consistency with a

previous QM/MM study on Pol *κ*.[40] A longer missing region in the palm domain (224–282) was replaced with a three-residue linker of Gln225, Ser226, and Gly281 using MODELLER[73, 74] incorporated into UCSF Chimera[41] (**Figure S1**). This was done as the longer missing residue could not be reasonably modeled. Previous data from a homolog of Pol *κ* indicates that the absence of the identified region does not impact the structural or functional features of the palm domain.[26, 42] The crystal structure was checked for clashes and protonated using MolProbity[43] after determining protonation states from PROPKA.[44, 45] The parameters for the incoming nucleotide (dCTP) and other nonstandard residues produced during the polymerization reaction were obtained from the R.E.D. Server,[46-49] while the missing bonded parameters were added by ANTECHAMBER[50, 51] (**Figure S2**). All the AMBER parameters for the non-standard residues are provided in the **Supporting Information**. The WT system was mutated *in silico* (Y432 to S) using the Dunbrack library of Chimera.[52] Both systems (WT and Y432S) were neutralized using K^+ ions and then solvated using a TIP3P[53] cubic water box of 88.3 x 101.7 x 94.2 $Å^3$, extending at least 12 Å from the surface of the protein-DNA complex with the LEaP module[54] of AMBER. The pmemd.cuda[55, 56] code from the AMBER18 suite was utilized to perform all MD simulations[57] with the ff14SB[58] and the OL15[59] force fields for the protein and the DNA, respectively. An initial minimization was performed for a total of 10,000 cycles, with 5,000 cycles using the steepest descent algorithm and the other 5,000 cycles using the conjugated gradient algorithm, followed by heating to 310 K using Langevin dynamics[60-62] with a collision frequency of 2 ps^{-1} and 100 kcal mol^{-1} $Å^{-2}$ restraint on all heavy atoms. Subsequently, 50 ns of NVT equilibration was applied to the systems, gradually reducing restraint on heavy atoms, while higher restraints were maintained on the 3′ terminal primer residue (dC3′) and dCTP until stability was achieved. Once equilibrated, each system was subjected to 500 ns of unrestrained NPT ensemble with a time step of 2fs. These steps were carried out in triplicates, resulting in a total of 1.5 μs simulation time (**Table S1**). All bonds involving hydrogen atoms were treated using SHAKE[63], and long-range Coulomb interactions[64] were handled with the smooth particle mesh Ewald method[65] with a 12 Å cutoff for non-bonded interactions.

The analysis of production dynamics, including root mean square deviations (RMSD), root mean square fluctuations (RMSF), and correlation matrices, was conducted using the CPPTRAJ module[66] of AMBER18 (**Figures S3**–**S8**). Normal mode analysis was also executed using the ProDy[67] code integrated into VMD.[68] Python libraries such as NumPy,[69, 70] Matplotlib,[71] Pandas,[72] statsmodels[73] module, and Gnuplot[74] command-line were employed for further data processing and graphing. Clustering was performed on 150,000 trajectories from all three replicates of each system through a multi-dimensional analysis via the *k*-means algorithm[75] implemented in AMBER's CPPTRAJ. Each dimension of this analysis on the reaction's active site corresponds to the distances and angles between the O3′ of dC3′ and the Pα of dCTP and other important distances of the coordinated residues to Mg^{2+} ions. Five representatives for each system with the highest population abundance and the best orientations of the active site's residues involved in the polymerization reaction were selected for further QM/MM optimizations (**Figures S9** & **S10**). PDB files of the representatives chosen for each system are provided as the **Supporting Information**.

2.2 QM/MM Calculations

All the QM/MM calculations of the studied systems were carried out via LICHEM,[76, 77] interfacing between Gaussian16[78] and TINKER.[79] The QM region and the MM environment were described with the ωB97X-D/6–31G(d,p)[80-82] level of theory and AMBER ff14SB force field, respectively. The QM/MM long-range electrostatic correction (QM/MM-LREC) method[83] with a 12 Å cutoff, and the particle mesh Ewald[64] (PME) method were employed for the QM subsystem and the MM calculations, respectively. The QM subsystem in both systems includes I106, D107, M108, D109, A110, D198, E199, dC3′, $dCTP^{3-}$/$dCTP^{4-}$, three Mg^{2+} cations, and coordinated water molecules to the metal ions (**Figure S11**). The total number of QM atoms for WT with five coordinated water molecules to the metal ions and Y432S with three coordinated water molecules to the metal ions are 152 and 146, respectively. The remaining residues and all solvent molecules were described with the ff14SB potential. To treat the covalent boundaries of the QM subsystem's amino acids, the pseudobond approach[84] was applied. The iterative QM/MM optimization protocol, as implemented in LICHEM76,[76, 77] involved optimizing all QM atoms and all MM atoms within a 30 Å radius of the catalytic Mg^{2+} ion (**Figure S11**). After optimizing each system's selected reactant representatives, the one with the lowest QM/MM energy was considered the most stable reactant, and the product was designed based on that structure (**Figures S9** & **S10**). Utilizing the optimized structures of reactants and products for each system, the quadratic string method (QSM) was employed in conjunction with the restrained-MM procedure, implemented in LICHEM,[77] to analyze and compare the potential energy surface along the reaction pathway. The initial restraint on the MM environment was initially set to 50 kcal mol^{-1} $Å^{-2}$ and gradually removed. The reaction path was modeled as a chain of fourteen beads connecting the reactant (bead 0) and the product (bead 15), totaling sixteen beads in the sequence. One negative imaginary frequency was obtained for the approximate transition states corresponding to the motion along the reaction coordinates (see **Movies S1–S3** in the **Supporting Information**).

2.3 NCI and ELF Analyses

The non-covalent interactions (NCI) between the incoming nucleotide and surrounding amino acids in the active site[85] were examined using the promolecular density method[86] incorporated into the Multiwfn V. 3.8 program.[87] This analysis provides a qualitative depiction of chemical bonding and weak noncovalent interactions by evaluating the relationship between electronic density and the reduced density gradient in regions of low electron density. The NCI surfaces' strength and characteristics are depicted in the RGB scale, with green and blue surfaces indicating strong and weak interactions, such as hydrogen bonds and van der Waals forces, while red surfaces signify repulsive interactions. These surfaces were visualized with the isovalue of 0.4 a.u and the color scale of -0.05 a.u < sign(λ_2)ρ < 0.05 a.u. All the wave functions for the electron localization function (ELF) analysis[88] were obtained from the structures of the reactant, product and the approximate TS optimized by the QM/MM calculations. The ELF calculations were performed via the basin analysis[89, 90] embedded in the Multiwfn V.3.8 program. A cubic grid of 200 a.u. with an isovalue of

0.8 a.u. and medium quality grid with a spacing of 0.10 Bohr were selected for the basin illustration. The images were rendered with visual molecular dynamics (VMD)[68] and GaussView 6.1[91] programs.

2.4 Energy Decomposition Analysis (EDA)

Calculation of the average energies of non-bonded intermolecular interactions (Coulomb + van der Waals) with respect to specific reference residue(s) can provide insight into the role of individual residues. EDA has been proven effective in exploring MD simulations and QM/MM calculations for various protein systems.[92-96] EDA was calculated using the AMBER-EDA code[97] on the pre-catalytic stage of the polymerization reaction by WT and Y432S systems, the analysis was run on 25000 snapshots of the last 500 ns of the MD simulations. The obtained results were then averaged over the three replicates of each system to qualitatively investigate the stabilizing and destabilizing effects of the amino acids. The R code V.4.1.2[98] and Python libraries, NumPy,[69, 70] Matplotlib,[71] and Pandas,[72] were used to generate and illustrate the EDA graphs. Sections 8 and 10 of the **Supporting Information** provide a comprehensive explanation of the calculation of the EDA and the interpretation of its results.

3 RESULTS AND DISCUSSION

3.1 Structural Effects of the Mutation

Experimental studies[99-104] and computational investigations[40, 105-114] on various eukaryotic and prokaryotic DNA polymerases have shown that the polymerization step is catalyzed via a two-metal-ion mechanism for these DNA polymerases. Lior-Hoffmann et al. revealed the importance of two metal ions for nucleotide addition by means of QM/MM-MD simulations.[40] Additionally, a recent ternary crystal structure of Pol κ in complex with DNA and a non-standard nucleotide obtained by Jha and Ling (PDB ID: 6CST) supports a two-metal-ion active site.[29]

Recently a third metal ion has been shown to be required during catalysis for two X- and one A-family DNA polymerases: Pol μ,[100] Pol η,[102, 115, 116] and Pol β.[103, 117, 118] QM/MM studies on Pol η[119, 120] and Pol β[121] have suggested that the third Mg^{2+} in the active site can either lower the activation barrier or stabilize the product primarily through its electrostatic effects. Yang et al.[122] and Nakamura et al.[123] also proposed that the third metal ion is a general feature, suggesting that all polymerization reactions of nucleic acids occur through three-metal-ion catalysis. Taking into account the outlined points on the importance of the third metal ion and to make a comparison with the mentioned-above QM/MM study on the two-metal-ion mechanism,[40] the three-metal-ion active site system was considered here for both the WT Pol κ and the Y432S variant (**Figure 1C**).

RMSD analysis, both for the backbone and by residue, indicates the stability of both systems throughout the 500 ns of MD simulations (**Figures S3–S8**). The RMSF analysis reveals mostly similar fluctuations between the WT and the mutant, with higher fluctuations observed in the N-clasp domain, as

well as some regions of the thumb and palm domains in the mutant (**Figure S12**). Notably, the palm and N-clasp domains play crucial roles in nucleotide addition and proper catalysis, respectively, making these increased fluctuations in the mutant, particularly intriguing. Similar results are suggested by dynamic cross-correlation analysis, wherein the motions within the N-clasp and palm domains, as well as their movement with respect to each other become less correlated (more anti-correlated) in the mutant compared to the WT (**Figure S13**).

Interestingly, no significant differences were observed in the motions within the PAD between the WT and the mutant. When considered alongside the similar RMSFs of the PAD in both the WT and the mutant—with minor fluctuations in some regions in the mutant—these results suggest that the mutation does not significantly affect the engagement of the protein with the DNA.

The motion of DNA is seen to be more correlated with the PAD domain in the WT, whereas the mutant shows a higher anti-correlation movement with the fingers and palm domains. The heatmap in **Figure 2A&B**, which depicts the correlation of residues with the incoming nucleotide as the reference, suggests that the movements of various domains in the WT system with respect to dCTP are comparable to those in the mutant, showing no significant differences.

Taken together, the RMSF, dynamic cross-correlation, and normal mode analyses suggest that the mutation has a minor structural effect on the Pol *κ* domains involved in protein-DNA complexation while exerting a more noticeable impact on domains responsible for stabilizing the ternary complex and engaging in nucleotide addition. Additionally, a clustering analysis focusing on the population distribution based on the catalytic distance and angle between dC3′ and dCTP suggests that most of the sample structures exhibit similar distances between Pα and O3′ for both the WT and the mutant (**Figures S9** and **S10**). Antczak et al. also suggested that the Y432S mutation does not significantly alter the structural features of the polymerase, increasing the Pα-O3′ distance by about 0.02Å on average from the WT, even though the active site and the metal positions show larger distortions.[39] This change in the active site and metal position might cause different coordination shells observed for the two systems studied here. The Y432S system showed more structural similarity to a mismatched (dG:dT) WT system. These findings suggest that despite the mentioned structural impacts of the mutant, it does not significantly affect the catalytic distance to the extent of rendering it catalytically incompetent.

In addition to the structural effects of the mutation on the dynamics of the reaction, the results of the EDA analysis also suggest its impact on the non-bonded interactions between the active site and the mutation site with the protein environment. As shown in **Figure S14**, several residues have considerable non-bonded interactions with the active site of both systems. However, some residues become more stabilizing or destabilizing in the mutant compared to the WT. Notably, the residues of the N-clasp and palm regions—where the mutation has more pronounced structural effects—are seen to exhibit larger changes to the non-bonded interactions with the active site of the mutant.

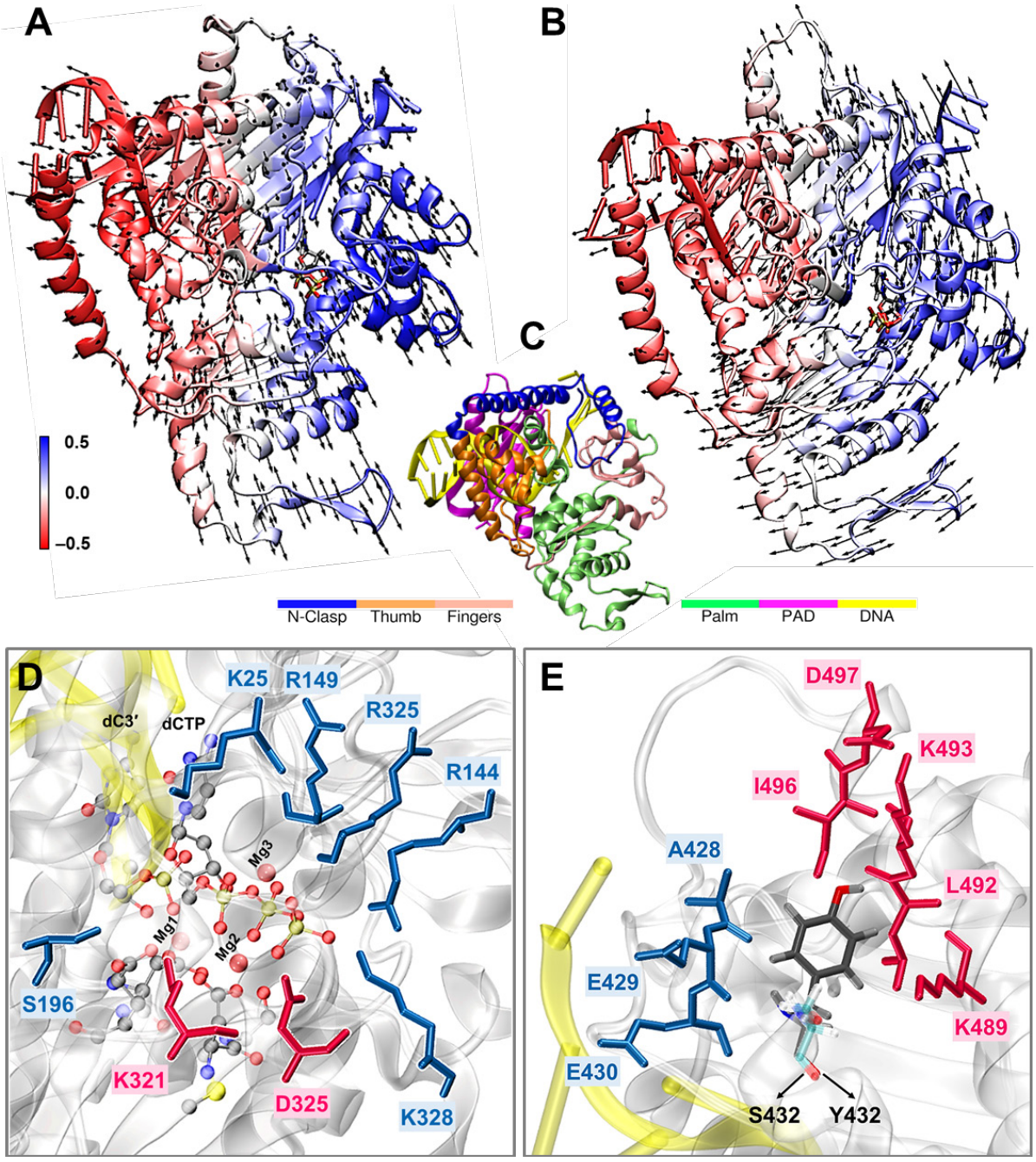

Figure 2. Plots of the principle component analysis on the root-mean-square fluctuations (first mode) along with the residue-wise correlation with respect to the incoming nucleotide as a heatmap projected on the protein for the **(A)** WT and **(B)** Y432S mutant. The black arrows show fluctuations more significant than 0.5 Å and point toward the direction of the highest-ranked eigenvector, and their amplitude is directly proportional to the length of the arrow. Areas with correlated movements in the heatmap are colored blue (0.5), non-correlated areas are white (0.0), and anti-correlated movements are red (−0.5). **(C)** A color-coded representation of Pol *κ* with a similar orientation to A and B for enhanced comparison of movements and domains. **(D)** Representation of the residues in the first- and second-shell with considerable stabilizing and destabilizing effects (colored in blue and red, respectively) on the mutant's active site compared to the WT. All H-atoms are omitted for more clarity. **(E)** A close-up of the residues with substantial stabilizing/destabilizing effects (depicted in blue/red) on the mutation site of the mutant compared to the WT. Residue S432 is displayed with a different color from Y432. The threshold for the selection is $\Delta E_{NB}^{Active\ site} \geq |10|$ kcal mol^{-1} (**Eq. S2**) and $\Delta E_{NB}^{432} \geq |0.5|$ kcal mol^{-1} (**Eq. S3**).

Figure 2D shows the residues in the first- and second-shell of the active site having considerable stabilizing or destabilizing effects on the mutant's active site compared with the WT. The calculated $\Delta E_{NB}^{Active\ site}$ values based on **Eq. S2** are presented in **Table S2**. Several residues around the active site, including K25, R144, R149, K182, S196, and K328, become more stabilizing (or less destabilizing) in the mutant. This stabilizing impact is reflected in the sum of the total difference in non-bonded intermolecular interactions between the WT and Y432S systems, i.e., $\sum\Delta E_{NB}^{Active\ site} \sim$ –174 kcal mol^{-1}. Although EDA is a qualitative tool, the considerable negative value of $\sum\Delta E_{NB}^{Active\ site}$ suggests a significant stabilizing effect from the protein's environment on the active site of the mutant compared to the WT. This might indicate that electronic changes in the protein's environment, particularly in the residues around the active site, become more favorable for the nucleotide binding, countering the mentioned structural effects imposed by the mutation.

Figure S15 shows that the major interactions of the mutation site residue are with the amino acids in its vicinity in the PAD domain with no considerable interactions observed with residues from other domains. **Figure 2E** shows the orientation of the residues with considerable stabilizing and destabilizing effects on residue 432 of the mutant compared to the WT. The calculated ΔE_{NB}^{432} values based on **Eq. S3** are listed in **Table S2**. As expected, the EDA results suggest that the mutation does not significantly change the total difference in the non-bonded interactions between either of these residues at the mutation site and the protein environment ($\sum\Delta E_{NB}^{432} = 5.4$ kcal mol^{-1}). However, the small positive value of $\sum\Delta E_{NB}^{432}$ shows slightly more destabilizing effects the mutant experiences than the WT at the mutation site.

3.2 Catalytic Effects of the Mutation

The mutation of Y to S at position 432 results in structural differences in the coordination mode of the Mg1 and Mg3 metal ions in the two systems. As schematically shown in **Figure 1D**, in the WT system, Mg1 is coordinated to D107, D198, E199, O3′ of dC3′, one of the Oα atoms of the dCTP, and a water molecule. Mg2 is coordinated to Oα, Oβ, and Oγ atoms of the dCTP, D107, M108, and D198, while Mg3 is coordinated to the Oα and Oγ atoms of the dCTP and four water molecules. In Y432S, Mg1 is coordinated to D107, D198, E199, O3′ of dC3′, one of the Oα atoms of the dCTP, and one of dC3′ phosphate bridge's oxygen. The coordination mode of Mg2 is similar to that in the WT, whereas Mg3 is coordinated to the Oα and Oγ atoms of the dCTP and one of the dC3′ phosphate bridge's oxygen. Based on the simulated dynamics, it appears that the distal effect of the mutation on the active site is orienting the dC3′ primer terminus in a manner that forces its phosphodiester oxygens to coordinate to Mg1 and Mg3. In contrast, in the WT, two water molecules fulfill this role.

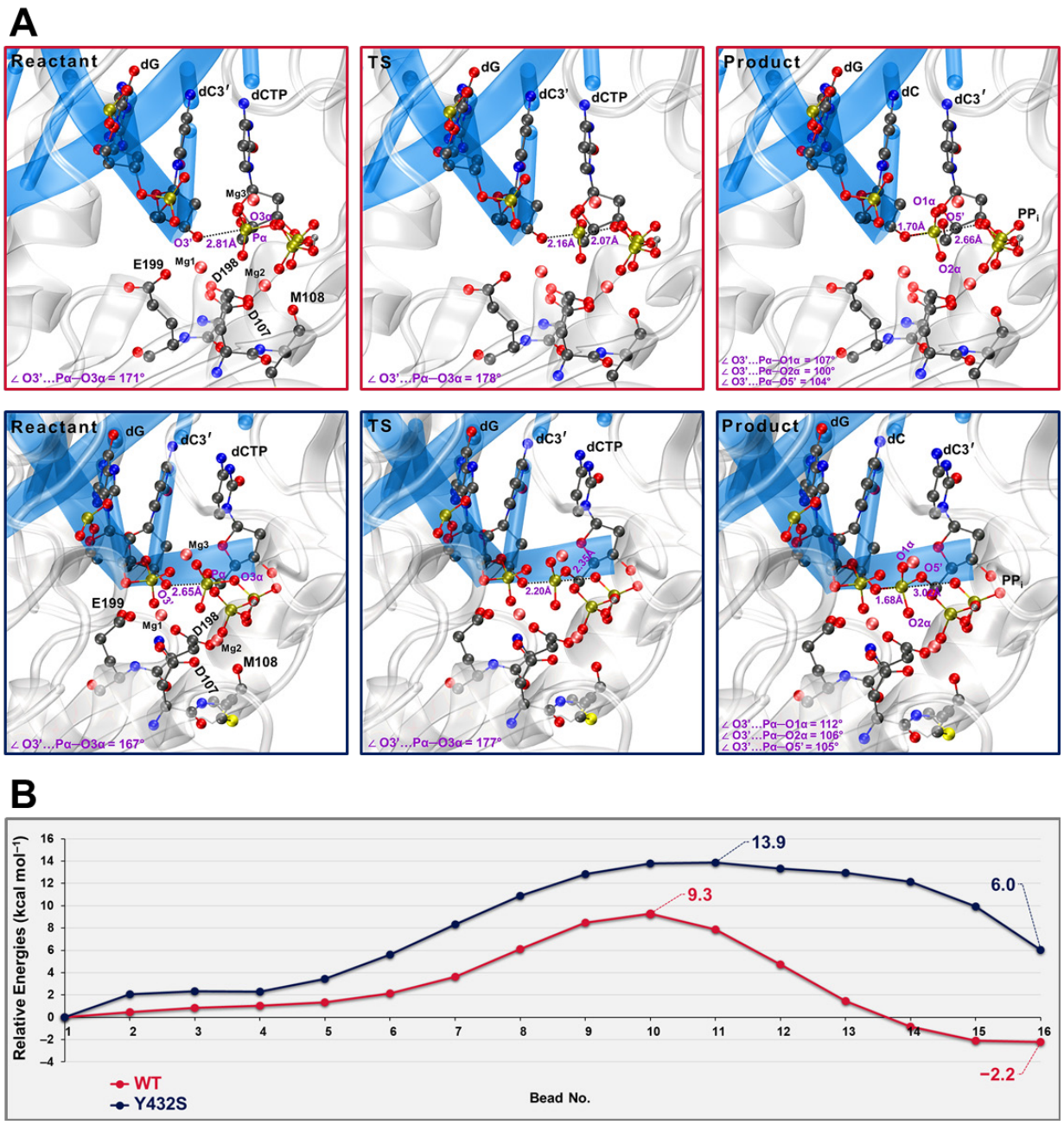

Figure 3. (A) Optimized geometries of the reactant, transition state, and product of the phosphoryl-transfer reaction in the active site of the WT Pol *κ* (top) and Y432S mutant (bottom). The protein and DNA chains are displayed in white and blue ribbons. The critical distances with the corresponding values are shown in dotted lines. **(B)** Optimized QM/MM minimum energy path (kcal mol^{-1}) for the catalytic reaction by each system calculated at ωB97X-D/6–31G(d,p) level of theory with AMBER ff14SB force field.

The catalytic O3′…Pα distances and O3′…Pα…O3α angles in the WT and the mutant's ternary complex are 2.81 Å and 2.65 Å, respectively, with corresponding angles of 171° and 167° (refer to **Figure 3A**). NCI index visualizations in **Figure 4A** also show green and blue surfaces between the O3′ of dC3′ and the Pα of dCTP in the reactant of both systems, indicating strong attraction interactions between them on the NCI scale. The activation energies (ΔE‡) are 9.3 and 13.9 kcal mol^{-1} for WT and Y432S, respectively,

suggesting a higher energetic barrier imposed by the mutation. The transition state in both systems is a pentacovalent phosphorane structure with the O3′…Pα…O3α angle close to 180°, which results from an S_N2-like nucleotidyl-transfer reaction, wherein the O3′–Pα bond forms, while the Pα–O3α bridge bond breaks (see **Movies S4** and **S5** in the **Supporting Information**). ELF calculations, illustrated in **Figure 4B**, also indicate the formation of two tri-synaptic basins in the transition state, corresponding to the O3′…Pα bond formation and the breaking of the Pα–Pβ bond. Calculated electron populations in the ELF basins (refer to **Table S3**) demonstrate the formation of (C3′,O3′,Pα) and (Pα,O3α,Pβ) trisynaptic basins during the reactant–TS pathway in both systems, each with an electron population of 2.74–3.15 e^-.

As depicted in **Figure 3A**, the geometry around the phosphorus atom in the new phosphodiester bridge is approximately tetrahedral. The electron populations for the newly formed (O3′,Pα) disynaptic basin are 1.78 e^- and 1.66 e^- in the WT and mutant, respectively, indicating the formation of an O3′–Pα single bond (see Figure **S16**). The produced PP_i in both systems' product exhibits multiple non-covalent attraction interactions with water molecules and residues around the active site's cavity, including D109, A110, F111, T138, R144, and K328 (in the mutant), as illustrated in **Figure S16**.

The catalytic reaction by WT is exoergic (ΔE = –2.2 kcal mol^{-1}), while the reaction by the mutant is endoergic (ΔE = 6.0 kcal mol^{-1}). The experimental k_{cat} values for the WT Pol *κ* range from 0.46 to 0.28 s^{-1}.[14, 16, 124, 125] According to transition state theory, the corresponding upper bound barrier for these k_{cat} values is ∼19 kcal mol^{-1}. Considering these observations, although both reactions are kinetically feasible, the product of the WT is ∼8 kcal mol^{-1} more stable than that of Y432S. This implies that the nucleophilic attack is thermodynamically more favorable in the WT.

As mentioned before, Lior-Hoffmann et al.[40] performed a comprehensive study of the two-metal-ion mechanism for the WT Pol *κ*, where they proposed that the phosphoryl-transfer step of the reaction with the $dCTP^{3-}$ is exergonic with the activation and reaction free energies of 10.6 and approximately –1.6 to –1.8 kcal mol^{-1}, respectively. Our calculated values mentioned above are consistent with these results. Nevertheless, it appears that the third magnesium ion has a non-negligible influence on the kinetics and thermodynamics of the reaction through its electrostatic effects (see below).

Compared with the WT, the changes induced by the mutation on both proximal and distal non-bonded interactions with the active site are consistent with the energetics results along the nucleophilic attack. EDA results suggest more stabilizing effects from the protein's environment on the Reactant to TS (R→TS) and Reactant to Product (R→P) pathways of WT Pol *κ* compared to the mutant. The values of $\sum\Delta E_{NB}^{TS-Reactant}$ (see **Eq. S4**) in **Figures S20** and **S21** indicating a stabilizing environment for the active site of WT, with a value of –23.1 kcal mol^{-1}. In contrast, the active site of Y432S experiences a destabilizing environment, as reflected by a value of 7.4 kcal mol^{-1}. It seems that the higher energy barrier for the mutant compared to the WT ($\Delta\Delta E^{\ddagger}$ = 4.6 kcal mol^{-1}) might at least partially come from the non-covalent effects of the protein's environment. The $\sum\Delta E_{NB}^{Product-Reactant}$ values (see **Eq. S4**) in **Figures S20** and **S21** are –136.0 kcal mol^{-1} for WT and –103.4 kcal mol^{-1} for Y432S. This indicates a consistent trend in the R→P pathway, with the

active site of WT experiencing a more stabilizing environment than the mutant. EDA results also suggest that residues R144, K321, and K328, located in the first- and second-coordination shell of the active site, play a crucial role in providing significant stabilizing contributions to the catalytic reaction in both systems (refer to **Figure S22**). These contributions are likely to facilitate the progress of the reaction.

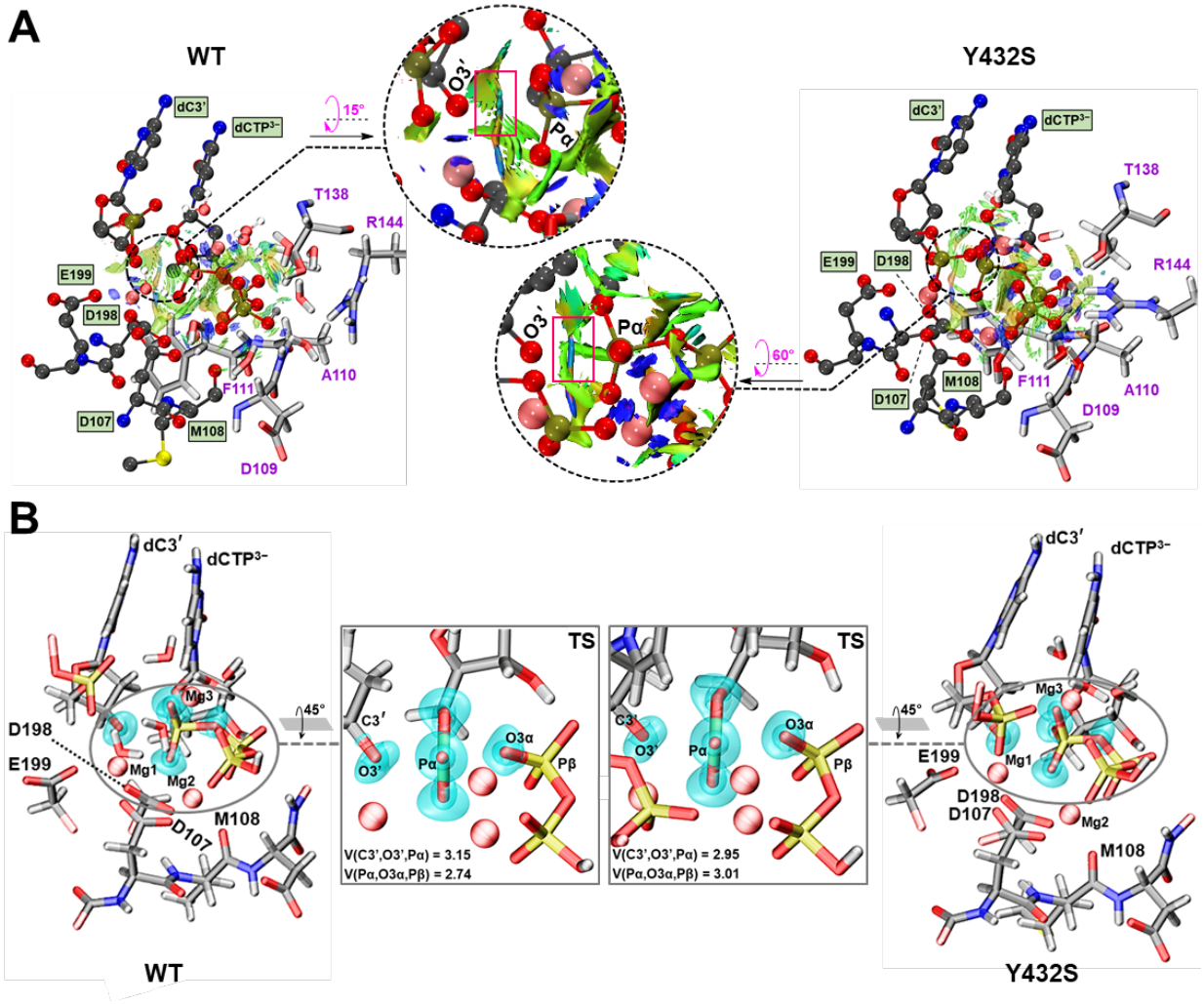

Figure 4. (A) Non-covalent interactions (NCI) between dCTP and surrounding residues in the reactant of WT and Y432S. Close-ups provide zoomed-in views of NCI surfaces between the O3′ of dC3′ and the Pα of dCTP. The NCI visualization uses an isovalue of 0.35 a.u, with a color scale of –0.05 a.u < sign(λ_2)ρ < 0.05 a.u. QM region residues are represented in ball-and-stick, while amino acids and water molecules are shown in sticks. The protein and hydrogen atoms of the QM residues are omitted for clarity. Coordinated water molecules to Mg atoms are distinguished by a different color from other water molecules. **(B)** ELF basins (isovalue = 0.8 a.u.) for the reactant and TS along the catalytic reaction pathway by the WT and Y432S. Zoomed-out images depict the reactant for each system, while zoomed-in frames show TS structures with values indicating trisynaptic basins for the critical forming/cleaving bonds.

Residues with significant differences in intermolecular interactions with the active site of the two systems along the R→TS and R→P catalytic pathways are shown in **Figure 5A**. As can be seen, in addition to those mentioned above that showed stabilizing contribution to the catalytic reaction pathway in both systems, several other residues become significantly more stabilizing or less destabilizing in the WT

compared to the mutant. Some of these residues with substantial $(\Delta\Delta E_{NB}^{WT-Y432S})_{TS/Product}$ values (see **Eq. S5**) are located in the first- and second shell of the active site, as illustrated in **Figure 5B**. These results also suggest that several residues around the active site, such as R144, L197, S310, D325, and K328, exhibit significant changes between the two systems along the R→TS and the R→P catalytic pathways in response to the distal tyrosine-to-serine mutation.

Residue R144 has a stabilizing effect on the active site of both systems along the R→TS pathway (**Figures S20** and **S21**), though this effect is more pronounced in the case of WT compared to the mutant, as reflected by the $(\Delta\Delta E_{NB}^{WT-Y432S})_{TS}$ of –2.6 kcal mol^{-1} in **Figure 5B**. This residue becomes particularly more stabilizing in the R→P pathway of both systems, with a more significant impact on the mutant system ($(\Delta\Delta E_{NB}^{WT-Y432S})_{Product}$ = 22.7 kcal mol^{-1}). Similar behavior can be observed from K328 with a stabilizing effect on the active site of both systems along the R→TS pathway but with a slightly larger impact on the WT ($(\Delta\Delta E_{NB}^{WT-Y432S})_{TS}$ = –2.4 kcal mol^{-1}). However, this effect becomes considerably more stabilizing in the mutant compared to the WT, as reflected by its $(\Delta\Delta E_{NB}^{WT-Y432S})_{Product}$ value of 15.8 kcal mol^{-1}.

Residues L197 and S310 exhibit different behavior with respect to the catalytic pathways of each system. L197 is stabilizing in the R→TS pathway of both systems, having a slightly larger effect on the mutant ($(\Delta\Delta E_{NB}^{WT-Y432S})_{TS}$ = 1.6 kcal mol^{-1}), while it becomes destabilizing in the R→P pathway of both, with more destructive contribution to the mutant ($(\Delta\Delta E_{NB}^{WT-Y432S})_{Product}$ = –2.2 kcal mol^{-1}). Residue S310 shows a similar trend as L197 with $(\Delta\Delta E_{NB}^{WT-Y432S})_{TS}$ and $(\Delta\Delta E_{NB}^{WT-Y432S})_{Product}$ values of 4.2 and –5.1 kcal mol^{-1}, respectively. Notably, D325 destabilizes the R→TS pathway of both systems, while its effect is less in the WT as reflected by $(\Delta\Delta E_{NB}^{WT-Y432S})_{TS}$ of –3.4 kcal mol^{-1}. However, this residue becomes significantly stabilizing in the R→P pathway of WT while still destabilizing the mutant, leading to a significant value of –12.5 for the $(\Delta\Delta E_{NB}^{WT-Y432S})_{Product}$.

Overall, the difference in intermolecular interactions between the two systems implies substantial facilitation of the catalytic reaction by the active site residues in the WT system. Furthermore, the EDA results for the catalytic reaction reveal that non-bonded contributions from the protein's environment enhance the thermodynamics of the reaction in both systems, with a more pronounced impact observed in the WT system. Conversely, the protein's environment, particularly the residues surrounding the active site (refer to values in **Figure 5B**), significantly destabilizes the transition state of the mutant, adversely affecting the kinetics of the reaction in the mutant system.

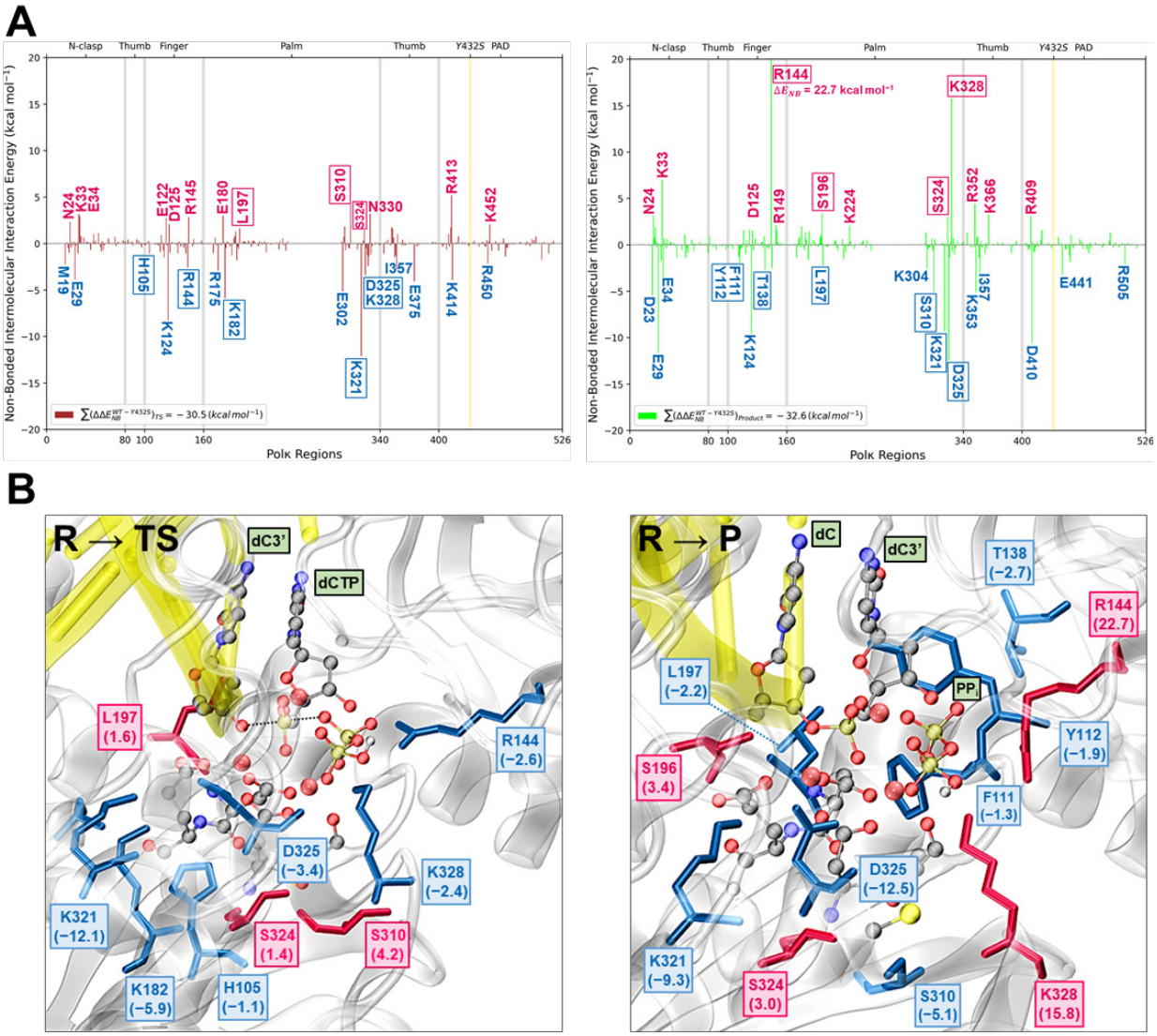

Figure 5. (A) The difference in non-bonded intermolecular interactions between the WT Pol *κ* and Y432S mutant systems along the R→TS (left) and the R→P (right) catalytic pathways. Residues with negative $(\Delta\Delta E_{NB}^{WT-Y432S})_{TS/Product}$ values in blue stabilize (or less destabilize) the active site of the WT compared to Y432S along the pathway of interest. In contrast, residues with positive $(\Delta\Delta E_{NB}^{WT-Y432S})_{TS/Product}$ values in red have the opposite effect (refer to Eq. S5). Residues given in frames are located in the active site's first- or second coordination shell. **(B)** Illustration of the first- and the second-coordination shell amino acids with a considerable difference of non-bonded intermolecular interactions with the active site. Residues in blue/red with negative/positive $(\Delta\Delta E_{NB}^{WT-Y432S})_{TS/Product}$ values in parenthesis (kcal mol^{-1}) stabilize/destabilize the active site of WT compared to Y432S system along the R→TS (left) and R→P (right) catalytic pathway. All hydrogen atoms, except the γ-hydrogen of dCTP, are omitted for more clarity.

3.3 Catalytic Effects of the Third Magnesium Ion

As discussed previously, recent structural findings highlight the involvement of a third metal ion in charge stabilization during the catalytic reactions in Pol *μ*, Pol *η*, and Pol *β*.[100, 102, 103, 115-118, 122, 123] A comparison of phosphoryl transfer initiation in two- versus three-metal-ion catalysis by Yang et al.[122] suggested that, in the latter, the third metal ion might initiate the reaction by breaking the existing

phosphodiester bond in dNTP, thereby driving the phosphoryl transfer reaction. Conversely, QM/MM studies on Pol *η* and Pol *β* suggest that a third Mg^{2+} in the active site may either lower the activation barrier or stabilize the product primarily through its electrostatic effects.[119-121]

To our knowledge, no study has investigated the catalytic polymerization reaction by Pol *κ* involving a third metal in the active site. As mentioned above, the 2OH2 PDB was chosen as the initial structure, which only involves one metal in the active site. For consistency with previous studies, the nucleotide-binding metal was included with the incoming nucleotide. Interestingly, during the MD simulations, the third metal was observed to diffuse to the active site in the initial stages, and remain bound to the triphosphate throughout the remainder of the simulations. The octahedral coordination mode of Mg1 and Mg2 in our modeled system aligns with their QM/MM–MD simulated structure; detailed stereochemistry is explained in **Section 3.2**. The third magnesium ion in our WT Pol *κ* modeled system is coordinated to the Oα and Oγ atoms of the dCTP and four water molecules (see **Figure 1D**).

While the QM/MM approaches utilized in the present study and the work by Lior-Hoffmann et al.[40] differ, the energy barriers (9.3 *vs.* 10.6 kcal mol^{-1}) and reaction energies (–2.2 vs. –1.6 to –1.8 kcal mol^{-1}) are consistent. Notably, the phosphorane transition state in both studies is stabilized by key amino acids, namely R144 and K328 (refer to **Figure S20A**). Our EDA results reveal that other residues, such as H105 and K321 in the binding cavity, stabilize the R→TS pathway despite lacking direct hydrogen bonding with the active site (see **Figure S22A**). The diffusion of the third magnesium into the active site appears to influence the geometries surrounding the dCTP phosphate chain through interactions with its Oα and Oγ atoms. This orientation of the phosphate chain not only sustains the direct and indirect (mediated by water molecules) hydrogen-bonding interactions with A110, T138, R144, and K328 (refer to **Figure 6A**) observed in the TS of the two-metal system,[40] but also gives rise to additional non-covalent interactions with D109 and water molecules, as illustrated in **Figure 6B**.

As previously noted, Yang et al.[122] proposed that the third metal ion might trigger the reaction in three-metal-ion catalysis by cleaving the pre-existing phosphodiester bond in dNTP, thereby initiating the phosphoryl-transfer reaction. However, our calculated ELF populations for all three systems in **Table S3** show no evidence of trisynaptic basins between Mg3 and phosphodiester bonds during the R→TS pathway. This suggests that the third magnesium is not directly involved in the bond-forming/breaking process in the studied systems. Notably, the active site orientation in the product of both WT systems (with $dCTP^{3-}$ and $dCTP^{4-}$) indicates non-covalent interactions between Mg3 and O3α, resulting in a distorted octahedral geometry around Mg3. Despite the Mg3…O3α distances of ~3.0 Å and the presence of green NCI surfaces between Mg3 and O3α (refer to **Figure 6C**), ELF results in **Table S3** indicate the creation of (O3α,Mg3) disynaptic basins in the products of WT–$dCTP^{3-}$ and WT–$dCTP^{4-}$, with electron populations of 2.97 e^- and 3.78 e^-, respectively.

In the Y432S product, a green NCI surface is observed between Mg3 and O3α. However, the distance of 3.58 Å prevents the formation of a disynaptic basin between them, as indicated in **Table S3**. This

maintains the product's octahedral geometry of the Mg3 stereocenter (see **Figure S23**). In addition to the formation of (O3α,Mg3) basin in the product of WT systems, (O2α,Mg3) and (O2γ,Mg3) disynaptic basins in all three systems (WT and Y432S) show considerable electron population increase along the R→TS→P catalytic pathway (refer to **Table S3**). This suggests that Mg3 may alleviate the accumulating negative charge on the O3α-bridging oxygen (only in WT), as well as on the O2γ and O2α oxygens, during the elongation and cleavage of the Pα–O3α bridge bond.

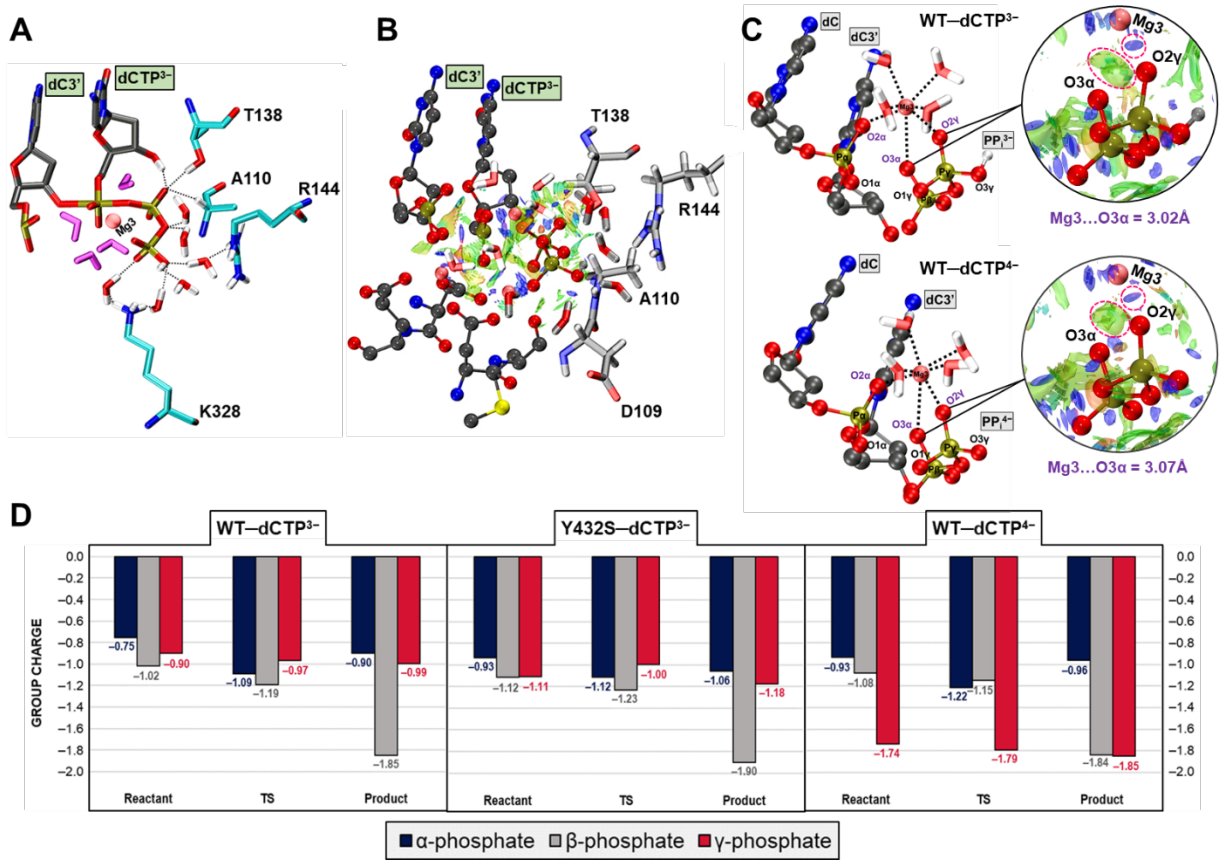

Figure 6. (A) Amino acids in the active site engaging in direct and indirect hydrogen-bonding interactions with the pentacovalent phosphorane transition state in the WT. Coordinated waters to Mg3 are displayed in purple to distinguish them from water molecules involved in hydrogen bonds. **(B)** NCI Surfaces in the transition state of WT–dCTP^{3-}: Interactions between the incoming nucleotide and surrounding residues. **(C)** Stereoview of the product in WT–dCTP^{3-} and WT–dCTP^{4-} systems, highlighting the geometry of the Mg3 stereocenter. Oxygen atoms coordinated to Mg3 are labeled in purple. Zoomed-in circles display NCI surfaces between Mg3 with O3α and O2γ atoms. **(D)** ESP charges for α-, β-, and γ-phosphate groups of dCTP at key stationary points in the catalytic reaction. The partial charge of the bridging oxygen atoms is evenly distributed among neighboring phosphate groups.

Calculated ESP charges for the reactants (**Figure 6D)** indicate that the γ-phosphate has the most negative partial charge among the phosphate groups of dCTP^{4-}, which is relieved in the protonated systems.[40, 126] The γ-phosphate's ESP charge in the WT–dCTP^{4-} system is –1.74 e^-, while the values for WT–dCTP^{3-} and Y432S–dCTP^{3-} are –0.90 e^- and –1.11 e^-, respectively. Notably, the ESP charge of the α-phosphate in the reactant of all three systems exhibits the lowest value compared to the other two phosphate groups. This may be attributed to the fact that the oxygens of the α-phosphate are coordinated

to all three metal centers, contributing to alleviating the negative charge. This alignment is further supported by the calculated electron populations in the (O1α,Mg1), (O1α,Mg2), and (O2α,Mg3) disynaptic basins in the reactants of all three systems, as detailed in **Table S3**. The ESP charges on the α-phosphate in the product of all three systems exhibit no significant differences (–0.90 to –1.06 e^-), likely attributable to the phosphoryl transfer and the formation of the newly established dC–dC3′ phosphodiester bridge. Comparing the total ESP charges on the pyrophosphates of the WT–dCTP^{3-} (2.8 e^-) and Y432S–dCTP^{3-} (3.1 e^-) systems and considering the formation of the (O3α,Mg3) basin in the former system's product, suggests that the third magnesium contributes more to the charge stabilization in the PPi product of the former system than in the latter.

Collectively, insights derived from non-covalent interaction analyses (EDA + NCI) and electronic population analyses (ELF + ESP) suggest that the third metal center positively influences the catalytic reaction in all three systems. This effect is likely a result of its electrostatic impact rather than direct participation in the bond-forming/breaking process.

3.4 Deprotonated dCTP as the Incoming Nucleotide

QM/MM studies on Pol *β*,[114, 115, 127, 128] Pol *λ*,[110, 129] and HIV reverse transcriptase[130] suggest protonated dNTPs (dNTP^{3-}) in the reactant of the catalytic reaction. Conversely, other experimental[99, 100, 102, 104, 116] and computational[40, 105-113, 119-121] investigations across various DNA polymerases support the incorporation of dNTPs in their deprotonated form (dNTP^{4-}) upon the formation of the ternary complex at pH ~7.0–7.5. Furthermore, in the various proposed mechanisms from the mentioned computational studies, the O3′ of the deprotonated 3′-end deoxyribose can attack the α-phosphate of either dNTP^{3-} or dNTP^{4-} during the chemistry step. The final by-product of the polymerization reaction in these studies can be either PP_i^{3-} or PP_i^{4-}.

In the scenario where PP_i^{3-} is usually the by-product, it is suggested that before the S_N2-like nucleophilic attack by O3′ on Pα, dNTP^{4-} can either directly absorb the proton from 3′-OH or utilizes a shuttle of mediating water molecules (see **Scheme 1A**&**B**). In a proposed mechanism by Genna et al., named the Self-Activated Mechanism, the proton can be transferred intramolecularly from the 3′-OH of dNTP^{4-} to its Pβ, also resulting in the formation of PP_i^{3-} as the by-product.[112] In the other scenario, where both PP_i^{3-} or PP_i^{4-} can be the by-products, the 3′-OH proton is absorbed by one of the conserved aspartate/glutamic acid residues in the active site, followed by the O3′ attacking the Pα of dNTP (see **Scheme 1C**).

Castro et al. have suggested that the transfer of two protons occurs in the chemistry step of several polymerases, involving the deprotonation of 3′-OH and the protonation of the leaving pyrophosphate.[131, 132] Thus, as elaborated above, the second proton transfer either might occur during the catalytic reaction or can be absorbed from ambient water after the release of PP_i^{4-}. Building on the discussed potential protonation states of dNTP and the resulting PP_i, we also conducted tests with deprotonated dCTP as the

incoming nucleotide (WT–dCTP^{4-} system) to understand better the impact of charge accumulation on the triphosphate group during the phosphorylation step.

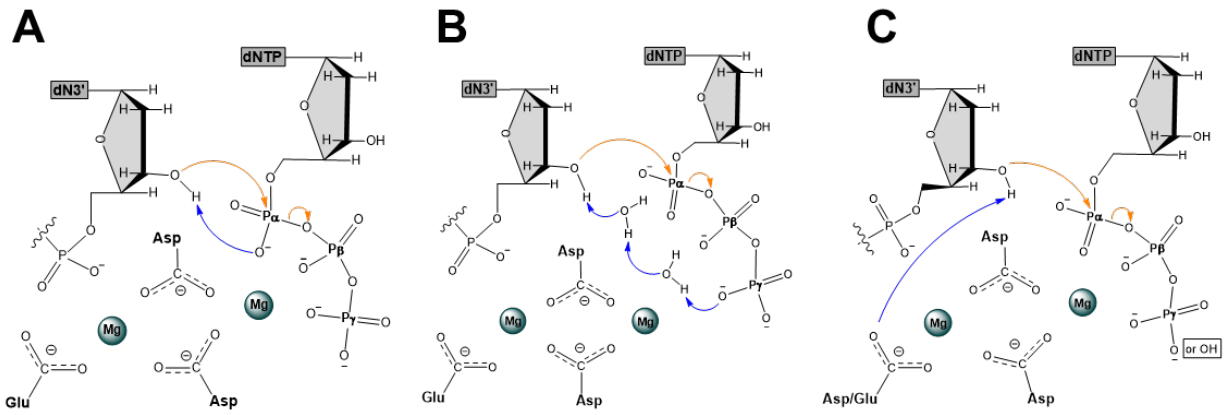

Scheme 1. Three commonly proposed mechanisms for the catalytic polymerization reaction by the DNA polymerases. Blue and orange arrows indicate proton transfers and S_N2 nucleophilic attack, respectively.

QM/MM and NCI results in **Figure 7** indicate that the orientation of the active site in the optimized reactant of WT–dCTP^{4-} is conducive to the catalytic reaction. The catalytic O3′…Pα distance and O3′…Pα…O3α angle in **Figure 7A** for the optimized reactant is 2.69 Å and 171°, respectively, favorable for an S_N2-like nucleotidyl transfer. Blue and green NCI surfaces in **Figure 7B** between the O3′ and Pα also suggest strong attraction interactions among these atoms, facilitating the nucleophilic attack. As depicted in **Figure 7B**, the optimized geometries of the reactant's active site with dCTP^{4-} resemble those observed with dCTP^{3-} (see **Figure 4A**). The primary distinction lies in the orientation of the water molecule involved in hydrogen bonding with the protonated/deprotonated Oγ.

As shown in **Figure 7A**, the energy barrier for WT–dCTP^{4-} is 7.9 kcal mol^{-1}, comparable with the 9.3 kcal mol^{-1} for WT–dCTP^{3-}. Similar with the other two systems, the transition state of WT–dCTP^{4-} exhibits a pentacovalent phosphorane structure arising from an S_N2-like nucleotidyl-transfer reaction (see **Movie S6** of the **Supporting Information**). The presence of trisynaptic basins with V(C3′,O3′,Pα) = 3.40 e^- and V(Pα,O3α,Pβ) = 2.73 e^- further indicates the formation and cleavage of O3′…Pα and Pα–Pβ bonds in the transition state (refer to **Table S3**). Notably, the reaction with dCTP^{3-} was exergonic (ΔE = –2.2 kcal mol^{-1}), while the reaction with dCTP^{4-} is slightly endergonic (ΔE = 0.7 kcal mol^{-1}). Although both reactions are kinetically feasible, considering the product with dCTP^{3-} is ~3 kcal mol^{-1} more stable than dCTP^{4-}, the nucleophilic attack seems more thermodynamically favorable with the protonated nucleotide.

The non-bonded interactions between Pol *κ* and the active site along the nucleophilic attack also suggest more stabilizing effects from the protein's environment on the reactant→ TS and reactant→ product pathways with dCTP^{3-} than dCTP^{4-}. The $\sum\Delta E_{NB}^{TS-Reactant}$ value of –23.1 kcal mol^{-1} (depicted in **Figure S20)** suggests a stabilizing environment for the active site of WT–dCTP^{3-}. Conversely, the active site of WT–dCTP^{4-}, similar to the mutant, encounters a destabilizing environment with a $\sum\Delta E_{NB}^{TS-Reactant}$ value of 14.5

kcal mol^{-1} in **Figure S24**. Similarly, the $\sum \Delta E_{NB}^{Product-Reactant}$ values in **Figures S20** and **S24** are –136.0 kcal mol^{-1} for WT–dCTP^{3-} and –91.4 kcal mol^{-1} for WT–dCTP^{4-}, respectively. This suggests a consistent pattern along the R→P pathway, where the active site of WT–dCTP^{3-} encounters a more stabilizing environment than WT–dCTP^{4-}.

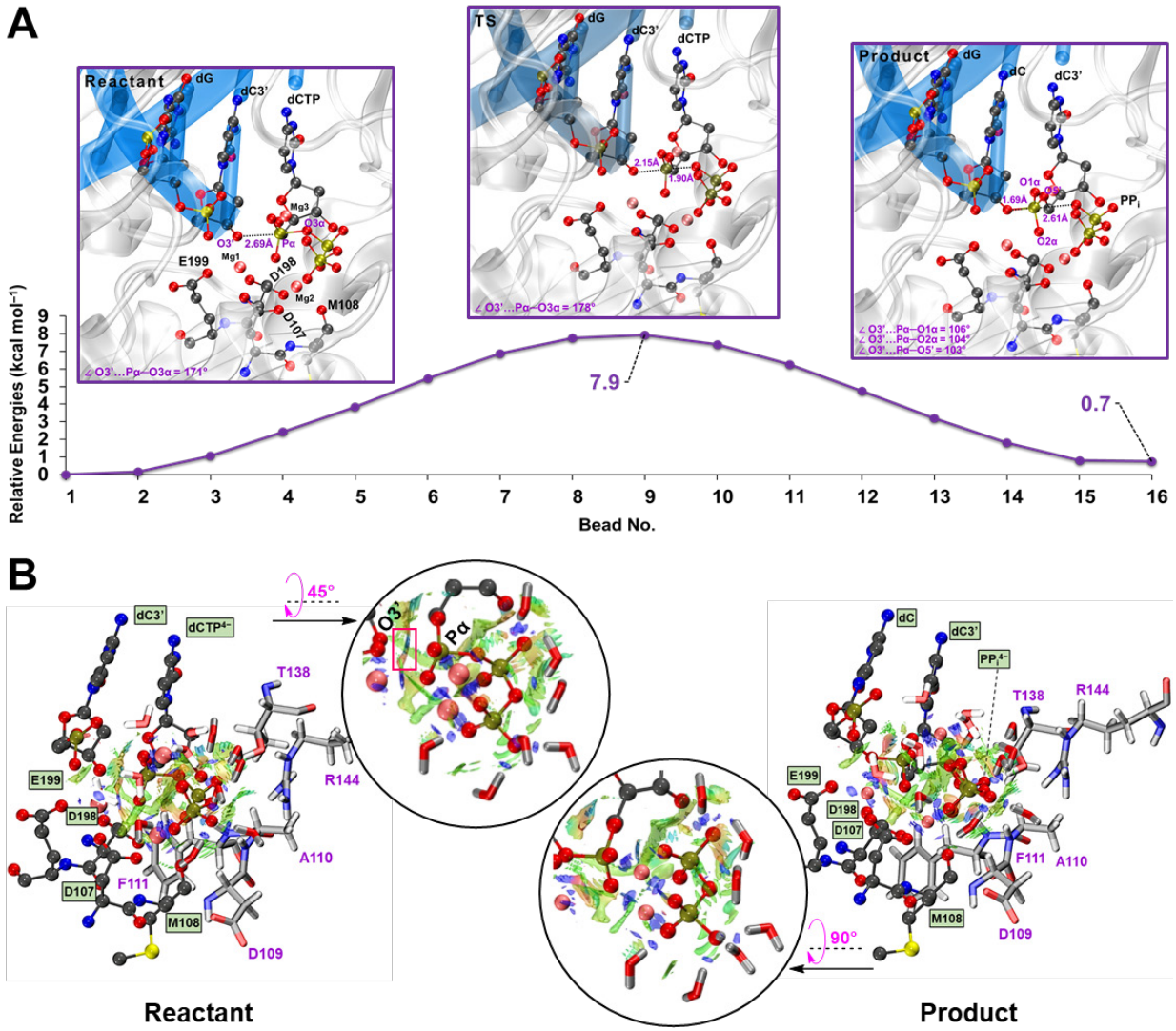

Figure 7. (A) Optimized QM/MM minimum energy pathway and optimized geometries for the reactant, TS, and product of the catalytic reaction by the WT with dCTP^{4-}. Structures are minimized at ωB97X-D/6–31G(d,p) level of theory with AMBER ff14SB force field. **(B)** NCI surfaces between the incoming nucleotide and surrounding residues in the reactant and product of WT–dCTP^{4-}. Close-up frames provide zoomed-in views of NCI surfaces for the phosphate chain of dCTP^{4-}.

Residues with significant differences in intermolecular interactions with the active site between WT–dCTP^{3-} and WT–dCTP^{4-} systems along the R→TS and R→P catalytic pathways are shown in **Figure 8A**. Residues R144, K321, and K328 demonstrate a notably more substantial stabilizing effect on the catalytic pathways in WT–dCTP^{3-} than in WT–dCTP^{4-}, consistent with the observed trend in the comparison between WT–dCTP^{3-} and the Y432S–dCTP^{3-}. Notably, the results in **Figure 8B** suggest that residues S310

and D325, situated in the active site's first- and second-coordination shell, respectively, exhibit significant changes in response to the protonation state of the nucleotide.

As shown in **Figures S20** and **S24**, D325 destabilizes the active site in both systems along the R→TS pathway. In contrast, this effect is much more noticeable in the case of dCTP^{4-} compared to dCTP^{3-} ($(\Delta\Delta E_{NB}^{dCTP^{3-}-dCTP^{4-}})_{TS}$ = –31.4 kcal mol^{-1}, see **Eq. S6**). Interestingly, D325 becomes considerably stabilizing in the R→P pathway of both system, with a larger impact observed in the case of dCTP^{3-} ($(\Delta\Delta E_{NB}^{dCTP^{3-}-dCTP^{4-}})_{Product}$ = –1.9 kcal mol^{-1}, see **Eq. S6**). Given the negatively charged character of D325 and its position in the second coordination shell of the active site, it exerts a destabilizing influence on the active site along the R→TS pathway. The accumulation of negative charge on dCTP^{4-} further amplifies this destabilizing effect. The alleviation of this destructive effect in the product is likely attributed to changes in charge distribution, as D325 does not engage in any hydrogen bonds with the active site residues.

In **Figures S20** and **S24**, it is shown that residue S310 exhibits a destabilizing effect on the R→TS pathway of WT–dCTP^{3-} while exerting a negligible stabilizing effect on WT–dCTP^{4-} ($(\Delta\Delta E_{NB}^{dCTP^{3-}-dCTP^{4-}})_{TS}$ = 4.1 kcal mol^{-1}). Remarkably, this effect does the opposite by considerably stabilizing the R→P pathway of WT–dCTP^{3-}, while significantly destabilizing WT–dCTP^{4-} ($(\Delta\Delta E_{NB}^{dCTP^{3-}-dCTP^{4-}})_{Product}$ = –12.0 kcal mol^{-1}). Taking into account the location of S310 in the first coordination shell of the active site (lacking hydrogen bonds with the nucleotide) and the lone pairs of the polar hydroxyl group in its side chain, this may elucidate its destabilizing impact on the transition state and product of the deprotonated nucleotide, attributed to an increased concentration of negative charge. Lin et al.[114] also argued that the excessive negative charge accumulation around the active site of Pol *β* with dTTP^{4-} leads to the formation of a highly negatively charged pyrophosphate product, which is unfavorable.

Collectively, the difference in intermolecular interactions between the two protonation states suggests that the active site residues significantly facilitate the catalytic reaction in favor of the protonated deoxycytidine triphosphate as the incoming nucleotide. Additionally, the EDA results for the catalytic reaction indicate that non-bonded contributions from the protein environment enhance the thermodynamics of the reaction in both systems, with a more pronounced impact observed in the WT–dCTP^{3-} system. However, the transition state of the WT–dCTP^{4-} is destabilized by the protein's environment, adversely affecting the kinetics of the reaction with the unprotonated nucleotide.

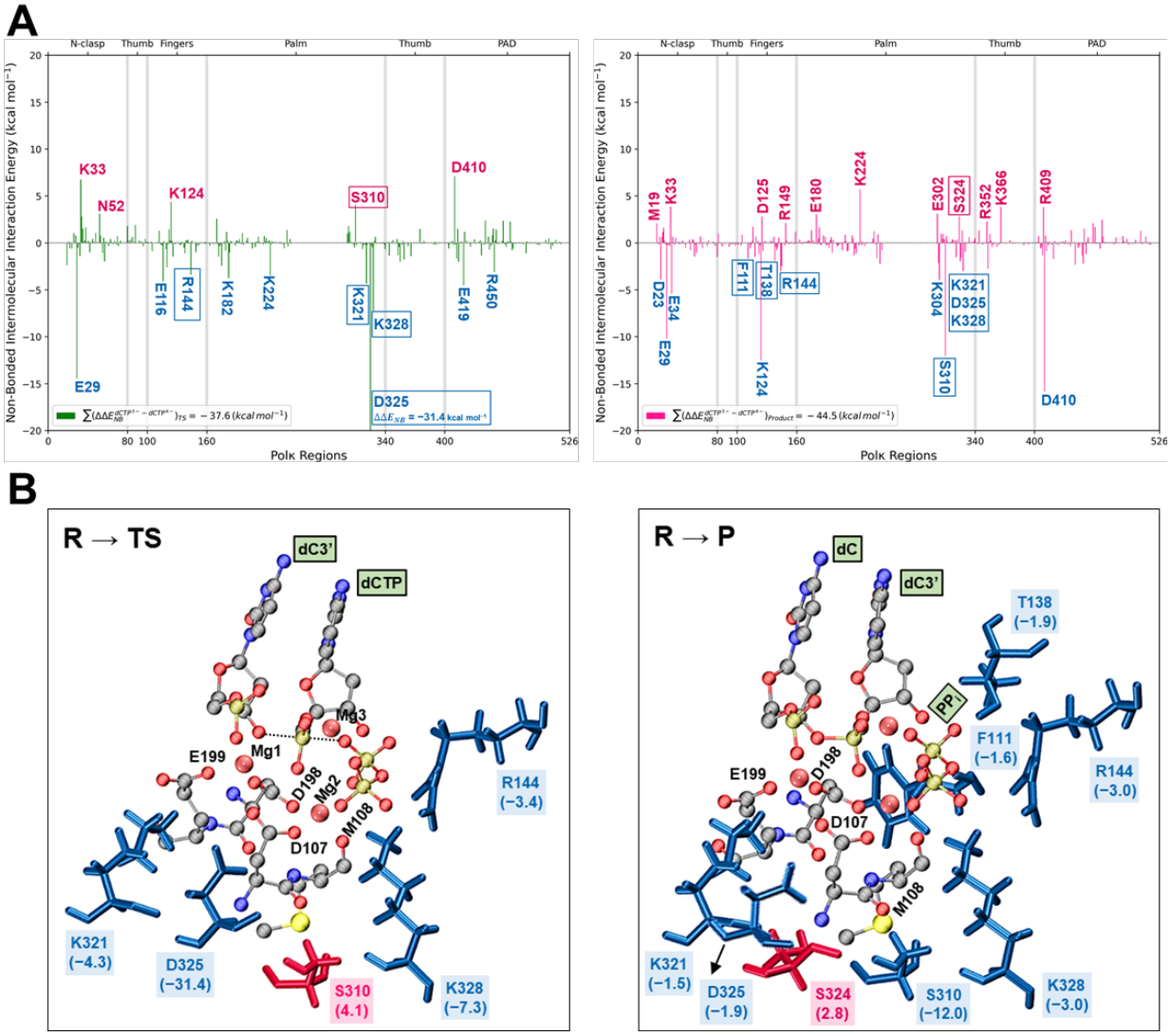

Figure 8. (A) The difference of non-bonded intermolecular interactions between the WT–dCTP^{3-} and WT–dCTP^{4-} systems along the R→TS (left) and the R→P (right) catalytic pathways. Residues with negative $(\Delta\Delta E_{NB}^{dCTP^{3-}-dCTP^{4-}})_{TS/Product}$ values in blue stabilize (or less destabilize) the active site of the WT–dCTP^{3-} compared to the WT–dCTP^{4-} system along the pathway of interest, while the residues in red have the opposite effect (see Eq. S6). Residues in frames are located in the first- or second-coordination shell of the active site. **(B)** Representation of the first- and second-coordination shell amino acids having considerable differences in non-bonded intermolecular interactions with the active site. Residues in blue/red with negative/positive $\Delta\Delta E_{NB}^{dCTP^{3-}-dCTP^{4-}}$ values in parenthesis (kcal mol^{-1}) stabilize/destabilize the active site of WT–dCTP^{3-} compared to WT–dCTP^{4-} along the R→TS (left) and R→P (right) catalytic pathway. The protein and DNA chains and the hydrogen atoms of the active site residues are not displayed for clarity.

4 CONCLUSION

In this study, molecular dynamics (MD) simulations and coupled quantum mechanics/molecular mechanics (QM/MM) optimizations were employed to study the mechanism of phosphoryl-transfer reaction with deoxycytidine triphosphate (dCTP) in the active site of WT Pol *κ* and its cancer-associated variant, Y432S. The characteristics of the three-metal-ion active site, the electrostatic effects of the third metal ion

(Mg3) on the catalytic reaction, and the influence of charge accumulation on the incoming nucleotide on the catalytic reaction were examined. The investigation of structural effects revealed intriguing dynamics within the protein's domains, suggesting that the mutation has a small impact on the structural integrity of Pol *κ* domains involved in protein-DNA complexation, but it more noticeably influences domains responsible for stabilizing the ternary complex and participating in nucleotide addition. The majority of the ensemble remains catalytically competent for both WT and mutant, highlighting the robustness of the polymerization process despite observed structural effects. Analysis of the pre-catalytic non-bonded interactions during the protein-DNA-nucleotide ternary complexation suggests a pronounced stabilizing effect from the protein's environment on the mutant's active site, confronting the structural effects caused by the mutation. The kinetics and thermodynamics of the catalytic reaction indicate that the mutation not only induces structural effects on the active site, altering the coordination mode of Mg1 and Mg3 metal ions, but also leads to higher activation/reaction energies of 13.9/6.0 kcal mol^{-1} for Y432S compared with 9.3/–2.2 kcal mol^{-1} for the WT, implying a less favorable nucleophilic attack in the mutant. Compared with a previous study on the two-metal-ion mechanism for the WT Pol *κ*, it appears that the electrostatic effects of the third magnesium in tandem with distal and proximal non-bonded interactions influence the kinetics and thermodynamics of the reaction catalyzed by the WT. The energetics and electronic results also suggest that the binding cavity residues play a crucial role in favoring the catalytic reaction with the protonated deoxycytidine triphosphate ($dCTP^{3-}$) as the incoming nucleotide compared to the deprotonated nucleotide ($dCTP^{4-}$). Results of the non-bonded interactions suggest that the contributions from the protein environment enhance the thermodynamics of the reaction in both systems, with a more significant impact in the WT–$dCTP^{3-}$ system, while the protein's environment destabilizes the transition state in the WT–$dCTP^{4-}$, adversely affecting the kinetics of the reaction with the unprotonated nucleotide. The results of this study on the effects of the Y432S variant on the dynamics and kinetics of the phosphoryl-transfer reaction in comparison to the WT Pol *κ* may provide valuable insights into the structural and functional aspects of this DNA polymerase variant and also the substantial electrostatic contribution of the third metal ion into the reaction.

ASSOCIATED CONTENT

Data Availability Statement

All simulations and analyses employed via third-party software are described and referenced in the Computational Methods section. The EDA and LICHEM software programs are available at the Cisneros Research Group GitHub: https://github.com/CisnerosResearch/AMBER-EDA and https://github.com/CisnerosResearch/LICHEM.

Supporting Information

The Supporting Information is available free of charge at

AMBER parameters for the non-standard residues, selected MD simulation representatives for each system, initial coordinates of the studied systems for the QM/MM optimizations, supplementary movies for the optimized reaction paths and the negative imaginary frequency for the approximate TSs (**ZIP**)

Additional details of MD simulation analysis, clustering, QM/MM path optimization, ESP charges, NCI, ELF and EDA (**PDF**)

ACKNOWLEDGMENTS

This study was funded by NIH Grant No. R01GM108583. The computational time for this project was provided by the University of North Texas CASCaM CRUNTCh3 high-performance cluster (partially funded by the NSF Grant Nos. CHE1531468 and OAC-2117247), by the NSF Extreme Science and Engineering Discovery Environment, XSEDE (Project No. TG-CHE160044), and the University of Texas at Dallas' Cyberinfrastructure and Research Services, Ganymede and Titan HPC clusters.

REFERENCES

1. Köhler, K.; Ferreira, P.; Pfander, B.; Boos, D., Regulation of the Initiation of DNA Replication Upon DNA Damage in Eukaryotes. *The Initiation of DNA Replication in Eukaryotes* **2016**, 443-460.

2. de Laat, W. L.; Jaspers, N. G.; Hoeijmakers, J. H., Molecular Mechanism of Nucleotide Excision Repair. *Genes & development* **1999**, *13*, 768-785.

3. Krokan, H. E.; Bjørås, M., Base Excision Repair. *Cold Spring Harbor perspectives in biology* **2013**, *5*, a012583.

4. Filée, J.; Forterre, P.; Sen-Lin, T.; Laurent, J., Evolution of DNA Polymerase Families: Evidences for Multiple Gene Exchange between Cellular and Viral Proteins. *Journal of molecular evolution* **2002**, *54*, 763-773.

5. Friedberg, E. C.; Walker, G. C.; Siede, W.; Wood, R. D., *DNA Repair and Mutagenesis*. American Society for Microbiology Press: 2005.

6. Sale, J. E.; Lehmann, A. R.; Woodgate, R., Y-Family DNA Polymerases and Their Role in Tolerance of Cellular DNA Damage. *Nature reviews Molecular cell biology* **2012**, *13*, 141-152.

7. Ohmori, H.; Friedberg, E. C.; Fuchs, R. P.; Goodman, M. F.; Hanaoka, F.; Hinkle, D.; Kunkel, T. A.; Lawrence, C. W.; Livneh, Z.; Nohmi, T., The Y-Family of DNA Polymerases. *Molecular cell* **2001**, *8*, 7-8.

8. Prakash, S.; Johnson, R. E.; Prakash, L., Eukaryotic Translesion Synthesis DNA Polymerases: Specificity of Structure and Function. *Annu. Rev. Biochem.* **2005**, *74*, 317-353.

9. Yang, W.; Woodgate, R., What a Difference a Decade Makes: Insights into Translesion DNA Synthesis. *Proceedings of the National Academy of Sciences* **2007**, *104*, 15591-15598.

10. Johnson, R. E.; Prakash, S.; Prakash, L., The Human Dinb1 Gene Encodes the DNA Polymerase Polθ. *Proceedings of the National Academy of Sciences* **2000**, *97*, 3838-3843.

11. Washington, M. T.; Johnson, R. E.; Prakash, L.; Prakash, S., Human Dinb1-Encoded DNA Polymerase K Is a Promiscuous Extender of Mispaired Primer Termini. *Proceedings of the National Academy of Sciences* **2002**, *99*, 1910-1914.

12. Rechkoblit, O.; Zhang, Y.; Guo, D.; Wang, Z.; Amin, S.; Krzeminsky, J.; Louneva, N.; Geacintov, N. E., Trans-Lesion Synthesis Past Bulky Benzo [a] Pyrene Diol Epoxide N2-Dg and N6-Da Lesions Catalyzed by DNA Bypass Polymerases. *Journal of Biological Chemistry* **2002**, *277*, 30488-30494.

13. Yasui, M.; Dong, H.; Bonala, R. R.; Suzuki, N.; Ohmori, H.; Hanaoka, F.; Johnson, F.; Grollman, A. P.; Shibutani, S., Mutagenic Properties of 3-(Deoxyguanosin-N 2-Yl)-2-Acetylaminofluorene, a Persistent Acetylaminofluorene-Derived DNA Adduct in Mammalian Cells. *Biochemistry* **2004**, *43*, 15005-15013.

14. Choi, J.-Y.; Angel, K. C.; Guengerich, F. P., Translesion Synthesis across Bulky N2-Alkyl Guanine DNA Adducts by Human DNA Polymerase K. *Journal of Biological Chemistry* **2006**, *281*, 21062-21072.

15. Poon, K.; Itoh, S.; Suzuki, N.; Laxmi, Y. S.; Yoshizawa, I.; Shibutani, S., Miscoding Properties of 6α-and 6β-Diastereoisomers of the N 2-(Estradiol-6-Yl)-2′-Deoxyguanosine DNA Adduct by Y-Family Human DNA Polymerases. *Biochemistry* **2008**, *47*, 6695-6701.

16. Choi, J.-Y.; Chowdhury, G.; Zang, H.; Angel, K. C.; Vu, C. C.; Peterson, L. A.; Guengerich, F. P., Translesion Synthesis across O6-Alkylguanine DNA Adducts by Recombinant Human DNA Polymerases. *Journal of Biological Chemistry* **2006**, *281*, 38244-38256.

17. Choi, J.-Y.; Guengerich, F. P., Kinetic Analysis of Translesion Synthesis Opposite Bulky N2-and O6-Alkylguanine DNA Adducts by Human DNA Polymerase Rev1. *Journal of Biological Chemistry* **2008**, *283*, 23645-23655.

18. Walsh, J. M.; Ippoliti, P. J.; Ronayne, E. A.; Rozners, E.; Beuning, P. J., Discrimination against Major Groove Adducts by Y-Family Polymerases of the Dinb Subfamily. *DNA repair* **2013**, *12*, 713-722.

19. Nevin, P.; Lu, X.; Zhang, K.; Engen, J. R.; Beuning, P. J., Noncognate DNA Damage Prevents the Formation of the Active Conformation of the Y-Family DNA Polymerases Dinb and DNA Polymerase K. *The FEBS journal* **2015**, *282*, 2646-2660.

20. Federley, R. G.; Romano, L. J., DNA Polymerase: Structural Homology, Conformational Dynamics, and the Effects of Carcinogenic DNA Adducts. *J Nucleic Acids* **2010**, *2010*.

21. Boudsocq, F.; Kokoska, R. J.; Plosky, B. S.; Vaisman, A.; Ling, H.; Kunkel, T. A.; Yang, W.; Woodgate, R., Investigating the Role of the Little Finger Domain of Y-Family DNA Polymerases in Low Fidelity Synthesis and Translesion Replication. *Journal of Biological Chemistry* **2004**, *279*, 32932-32940.

22. Pata, J. D., Structural Diversity of the Y-Family DNA Polymerases. *Biochimica et Biophysica Acta (BBA)-Proteins and Proteomics* **2010**, *1804*, 1124-1135.

23. Goodman, M. F.; Woodgate, R., Translesion DNA Polymerases. *Cold Spring Harbor perspectives in biology* **2013**, *5*, a010363.

24. Wilson, R. C.; Jackson, M. A.; Pata, J. D., Y-Family Polymerase Conformation Is a Major Determinant of Fidelity and Translesion Specificity. *Structure* **2013**, *21*, 20-31.

25. Zahurancik, W. J.; Baranovskiy, A. G.; Tahirov, T. H.; Suo, Z., Comparison of the Kinetic Parameters of the Truncated Catalytic Subunit and Holoenzyme of Human DNA Polymerase Varepsilon. *DNA Repair (Amst)* **2015**, *29*, 16-22.

26. Uljon, S. N.; Johnson, R. E.; Edwards, T. A.; Prakash, S.; Prakash, L.; Aggarwal, A. K., Crystal Structure of the Catalytic Core of Human DNA Polymerase Kappa. *Structure* **2004**, *12*, 1395-1404.

27. Lancey, C.; Tehseen, M.; Bakshi, S.; Percival, M.; Takahashi, M.; Sobhy, M. A.; Raducanu, V. S.; Blair, K.; Muskett, F. W.; Ragan, T. J., Cryo-Em Structure of Human Pol K Bound to DNA and Mono-Ubiquitylated Pcna. *Nature Communications* **2021**, *12*, 6095.

28. Jia, L.; Geacintov, N. E.; Broyde, S., The N-Clasp of Human DNA Polymerase Kappa Promotes Blockage or Error-Free Bypass of Adenine- or Guanine-Benzo[a]Pyrenyl Lesions. *Nucleic Acids Res* **2008**, *36*, 6571-84.

29. Jha, V.; Ling, H., 2.0 Å Resolution Crystal Structure of Human Polκ Reveals a New Catalytic Function of N-Clasp in DNA Replication. *Scientific reports* **2018**, *8*, 15125.

30. Lone, S.; Townson, S. A.; Uljon, S. N.; Johnson, R. E.; Brahma, A.; Nair, D. T.; Prakash, S.; Prakash, L.; Aggarwal, A. K., Human DNA Polymerase K Encircles DNA: Implications for Mismatch Extension and Lesion Bypass. *Molecular cell* **2007**, *25*, 601-614.

31. Stern, H. R.; Sefcikova, J.; Chaparro, V. E.; Beuning, P. J., Mammalian DNA Polymerase Kappa Activity and Specificity. *Molecules* **2019**, *24*, 2805.

32. Kim, J. K.; Yeom, M.; Hong, J. K.; Song, I.; Lee, Y. S.; Guengerich, F. P.; Choi, J. Y., Six Germline Genetic Variations Impair the Translesion Synthesis Activity of Human DNA Polymerase Kappa. *Chem Res Toxicol* **2016**, *29*, 1741-1754.

33. Niimi, N.; Sassa, A.; Katafuchi, A.; Grúz, P.; Fujimoto, H.; Bonala, R.-R.; Johnson, F.; Ohta, T.; Nohmi, T., The Steric Gate Amino Acid Tyrosine 112 Is Required for Efficient Mismatched-Primer Extension by Human DNA Polymerase K. *Biochemistry* **2009**, *48*, 4239-4246.

34. Liu, Y.; Yang, Y.; Tang, T.-S.; Zhang, H.; Wang, Z.; Friedberg, E.; Yang, W.; Guo, C., Variants of Mouse DNA Polymerase K Reveal a Mechanism of Efficient and Accurate Translesion Synthesis Past a Benzo [a] Pyrene Dg Adduct. *Proceedings of the National Academy of Sciences* **2014**, *111*, 1789-1794.

35. Liu, Y.; Ma, X.; Guo, C., Effects of the N Terminus of Mouse DNA Polymerase K on the Bypass of a Guanine-Benzo [a] Pyrenyl Adduct. *The journal of biochemistry* **2016**, *159*, 471-479.

36. Swett, R. J.; Elias, A.; Miller, J. A.; Dyson, G. E.; Andres Cisneros, G., Hypothesis Driven Single Nucleotide Polymorphism Search (Hydn-Snp-S). *DNA Repair (Amst)* **2013**, *12*, 733-40.

37. Shao, M.; Jin, B.; Niu, Y.; Ye, J.; Lu, D.; Han, B., Association of Polk Polymorphisms with Platinum-Based Chemotherapy Response and Severe Toxicity in Non-Small Cell Lung Cancer Patients. *Cell Biochem Biophys* **2014**, *70*, 1227-37.

38. Song, I.; Kim, E. J.; Kim, I. H.; Park, E. M.; Lee, K. E.; Shin, J. H.; Guengerich, F. P.; Choi, J. Y., Biochemical Characterization of Eight Genetic Variants of Human DNA Polymerase Kappa Involved in Error-Free Bypass across Bulky N(2)-Guanyl DNA Adducts. *Chem Res Toxicol* **2014**, *27*, 919-30.

39. Antczak, N. M.; Walker, A. R.; Stern, H. R.; Leddin, E. M.; Palad, C.; Coulther, T. A.; Swett, R. J.; Cisneros, G. A.; Beuning, P. J., Characterization of Nine Cancer-Associated Variants in Human DNA Polymerase Kappa. *Chem Res Toxicol* **2018**, *31*, 697-711.

40. Lior-Hoffmann, L.; Wang, L.; Wang, S.; Geacintov, N. E.; Broyde, S.; Zhang, Y., Preferred Wmsa Catalytic Mechanism of the Nucleotidyl Transfer Reaction in Human DNA Polymerase K Elucidates Error-Free Bypass of a Bulky DNA Lesion. *Nucleic acids research* **2012**, *40*, 9193-9205.

41. Pettersen, E. F.; Goddard, T. D.; Huang, C. C.; Couch, G. S.; Greenblatt, D. M.; Meng, E. C.; Ferrin, T. E., Ucsf Chimera—a Visualization System for Exploratory Research and Analysis. *Journal of computational chemistry* **2004**, *25*, 1605-1612.

42. Jia, L.; Geacintov, N. E.; Broyde, S., The N-Clasp of Human DNA Polymerase K Promotes Blockage or Error-Free Bypass of Adenine-or Guanine-Benzo [a] Pyrenyl Lesions. *Nucleic acids research* **2008**, *36*, 6571-6584.

43. Chen, V. B.; Arendall, W. B.; Headd, J. J.; Keedy, D. A.; Immormino, R. M.; Kapral, G. J.; Murray, L. W.; Richardson, J. S.; Richardson, D. C., Molprobity: All-Atom Structure Validation for Macromolecular Crystallography. *Acta Crystallographica Section D: Biological Crystallography* **2010**, *66*, 12-21.

44. Olsson, M. H.; Sondergaard, C. R.; Rostkowski, M.; Jensen, J. H., Propka3: Consistent Treatment of Internal and Surface Residues in Empirical Pka Predictions. *J Chem Theory Comput* **2011**, *7*, 525-37.

45. Sondergaard, C. R.; Olsson, M. H.; Rostkowski, M.; Jensen, J. H., Improved Treatment of Ligands and Coupling Effects in Empirical Calculation and Rationalization of Pka Values. *J Chem Theory Comput* **2011**, *7*, 2284-95.

46. Bayly, C. I.; Cieplak, P.; Cornell, W. D.; Kollman, P. A., A Well-Behaved Electrostatic Potential Based Method Using Charge Restraints for Deriving Atomic Charges - the Resp Model. *J Phys Chem-Us* **1993**, *97*, 10269-10280.

47. Dupradeau, F.-Y.; Pigache, A.; Zaffran, T.; Savineau, C.; Lelong, R.; Grivel, N.; Lelong, D.; Rosanski, W.; Cieplak, P., The Red. Tools: Advances in Resp and Esp Charge Derivation and Force Field Library Building. *Physical Chemistry Chemical Physics* **2010**, *12*, 7821-7839.

48. Vanquelef, E.; Simon, S.; Marquant, G.; Garcia, E.; Klimerak, G.; Delepine, J. C.; Cieplak, P.; Dupradeau, F. Y., Red Server: A Web Service for Deriving Resp and Esp Charges and Building Force Field Libraries for New Molecules and Molecular Fragments. *Nucleic Acids Research* **2011**, *39*, W511-W517.

49. Wang, F.; Becker, J.-P.; Cieplak, P.; Dupradeau, F.-Y. Red Python: Object Oriented Programming for Amber Force Fields. In Abstracts of Papers of the American Chemical Society, 2014; AMER CHEMICAL SOC 1155 16TH ST, NW, WASHINGTON, DC 20036 USA: 2014; Vol. 247.

50. Wang, J.; Wolf, R. M.; Caldwell, J. W.; Kollman, P. A.; Case, D. A., Development and Testing of a General Amber Force Field. *J Comput Chem* **2004**, *25*, 1157-74.

51. Wang, J.; Wang, W.; Kollman, P. A.; Case, D. A., Automatic Atom Type and Bond Type Perception in Molecular Mechanical Calculations. *J Mol Graph Model* **2006**, *25*, 247-60.

52. Dunbrack Jr, R. L., Rotamer Libraries in the 21st Century. *Current opinion in structural biology* **2002**, *12*, 431-440.

53. Jorgensen, W. L.; Chandrasekhar, J.; Madura, J. D.; Impey, R. W.; Klein, M. L., Comparison of Simple Potential Functions for Simulating Liquid Water. *J Chem Phys* **1983**, *79*, 926-935.

54. Schafmeister, C.; Ross, W.; Romanovski, V., Leap. *University of California, San Francisco* **1995**.

55. Le Grand, S.; Götz, A. W.; Walker, R. C., Spfp: Speed without Compromise—a Mixed Precision Model for Gpu Accelerated Molecular Dynamics Simulations. *Computer Physics Communications* **2013**, *184*, 374-380.

56. Xu, D.; Williamson, M. J.; Walker, R. C. Advancements in Molecular Dynamics Simulations of Biomolecules on Graphical Processing Units. In *Annual Reports in Computational Chemistry*; Elsevier: 2010; Vol. 6, pp 2-19.

57. Case, D.; Ben-Shalom, I.; Brozell, S.; Cerutti, D.; Cheatham III, T.; Cruzeiro, V.; Darden, T.; Duke, R.; Ghoreishi, D.; Gilson, M., Amber 2018, Univ. *California, San Fr* **2018**.

58. Maier, J. A.; Martinez, C.; Kasavajhala, K.; Wickstrom, L.; Hauser, K. E.; Simmerling, C., Ff14sb: Improving the Accuracy of Protein Side Chain and Backbone Parameters from Ff99sb. *J Chem Theory Comput* **2015**, *11*, 3696-713.

59. Zgarbová, M.; Sponer, J.; Otyepka, M.; Cheatham III, T. E.; Galindo-Murillo, R.; Jurecka, P., Refinement of the Sugar–Phosphate Backbone Torsion Beta for Amber Force Fields Improves the Description of Z-and B-DNA. *Journal of chemical theory and computation* **2015**, *11*, 5723-5736.

60. Zwanzig, R., Nonlinear Generalized Langevin Equations. *Journal of Statistical Physics* **1973**, *9*, 215-220.

61. Loncharich, R. J.; Brooks, B. R.; Pastor, R. W., Langevin Dynamics of Peptides: The Frictional Dependence of Isomerization Rates of N-Acetylalanyl-N'-Methylamide. *Biopolymers* **1992**, *32*, 523-35.

62. Gillespie, D. T., The Chemical Langevin Equation. *J Chem Phys* **2000**, *113*, 297-306.

63. Ryckaert, J.-P.; Ciccotti, G.; Berendsen, H. J., Numerical Integration of the Cartesian Equations of Motion of a System with Constraints: Molecular Dynamics of N-Alkanes. *Journal of computational physics* **1977**, *23*, 327-341.

64. Essmann, U.; Perera, L.; Berkowitz, M. L.; Darden, T.; Lee, H.; Pedersen, L. G., A Smooth Particle Mesh Ewald Method. *J Chem Phys* **1995**, *103*, 8577-8593.

65. Salomon-Ferrer, R.; Gotz, A. W.; Poole, D.; Le Grand, S.; Walker, R. C., Routine Microsecond Molecular Dynamics Simulations with Amber on Gpus. 2. Explicit Solvent Particle Mesh Ewald. *Journal of chemical theory and computation* **2013**, *9*, 3878-3888.

66. Roe, D. R.; Cheatham III, T. E., Ptraj and Cpptraj: Software for Processing and Analysis of Molecular Dynamics Trajectory Data. *Journal of chemical theory and computation* **2013**, *9*, 3084-3095.

67. Bakan, A.; Meireles, L. M.; Bahar, I., Prody: Protein Dynamics Inferred from Theory and Experiments. *Bioinformatics* **2011**, *27*, 1575-7.

68. Humphrey, W.; Dalke, A.; Schulten, K., Vmd: Visual Molecular Dynamics. *J Mol Graph* **1996**, *14*, 33-8, 27-8.

69. Oliphant, T. E., *A Guide to Numpy*. Trelgol Publishing USA: 2006; Vol. 1.

70. Van Der Walt, S.; Colbert, S. C.; Varoquaux, G., The Numpy Array: A Structure for Efficient Numerical Computation. *Computing in science & engineering* **2011**, *13*, 22-30.

71. Hunter, J. D., Matplotlib: A 2d Graphics Environment. *Computing in Science & Engineering* **2007**, *9*, 90-95.

72. McKinney, W. Data Structures for Statistical Computing in Python. In Proceedings of the 9th Python in Science Conference, 2010; Austin, TX: 2010; Vol. 445; pp 51-56.

73. Seabold, S.; Perktold, J. Statsmodels: Econometric and Statistical Modeling with Python. In Proceedings of the 9th Python in Science Conference, 2010; Austin, TX: 2010; Vol. 57; p 61.

74. Williams, T.; Kelley, C.; Broker, H.; John Campbell, R.; Cunningham, D.; Denholm, G.; Elber, R.; Fearick, C.; Grammes, L.; Hart, L., In; 2019.

75. Likas, A.; Vlassis, N.; Verbeek, J. J., The Global

-Means Clustering Algorithm. *Pattern Recogn* **2003**, *36*, 451-461.

76. Kratz, E. G.; Walker, A. R.; Lagardere, L.; Lipparini, F.; Piquemal, J. P.; Andres Cisneros, G., Lichem: A Qm/Mm Program for Simulations with Multipolar and Polarizable Force Fields. *J Comput Chem* **2016**, *37*, 1019-29.

77. Gokcan, H.; Vazquez-Montelongo, E. A.; Cisneros, G. A., Lichem 1.1: Recent Improvements and New Capabilities. *J Chem Theory Comput* **2019**, *15*, 3056-3065.

78. Frisch, M. J.; Trucks, G. W.; Schlegel, H. B.; Scuseria, G. E.; Robb, M. A.; Cheeseman, J. R.; Scalmani, G.; Barone, V.; Petersson, G. A.; Nakatsuji, H.; Li, X.; Caricato, M.; Marenich, A. V.; Bloino, J.; Janesko, B. G.; Gomperts, R.; Mennucci, B.; Hratchian, H. P.; Ortiz, J. V.; Izmaylov, A. F.; Sonnenberg, J. L.; Williams; Ding, F.; Lipparini, F.; Egidi, F.; Goings, J.; Peng, B.; Petrone, A.; Henderson, T.; Ranasinghe, D.; Zakrzewski, V. G.; Gao, J.; Rega, N.; Zheng, G.; Liang, W.; Hada, M.; Ehara, M.; Toyota, K.; Fukuda, R.; Hasegawa, J.; Ishida, M.; Nakajima, T.; Honda, Y.; Kitao, O.; Nakai, H.; Vreven, T.; Throssell, K.; Montgomery Jr., J. A.; Peralta, J. E.; Ogliaro, F.; Bearpark, M. J.; Heyd, J. J.; Brothers, E. N.; Kudin, K. N.; Staroverov, V. N.; Keith, T. A.; Kobayashi, R.; Normand, J.; Raghavachari, K.; Rendell, A. P.; Burant, J. C.; Iyengar, S. S.; Tomasi, J.; Cossi, M.; Millam, J. M.; Klene, M.; Adamo, C.; Cammi, R.; Ochterski, J. W.; Martin, R. L.; Morokuma, K.; Farkas, O.; Foresman, J. B.; Fox, D. J. *Gaussian 16 Rev. C.01*, Wallingford, CT, 2016.

79. Rackers, J. A.; Wang, Z.; Lu, C.; Laury, M. L.; Lagardere, L.; Schnieders, M. J.; Piquemal, J. P.; Ren, P.; Ponder, J. W., Tinker 8: Software Tools for Molecular Design. *J Chem Theory Comput* **2018**, *14*, 5273-5289.

80. Chai, J.-D.; Head-Gordon, M., Long-Range Corrected Hybrid Density Functionals with Damped Atom–Atom Dispersion Corrections. *Physical Chemistry Chemical Physics* **2008**, *10*, 6615-6620.

81. Hariharan, P. C.; Pople, J. A., The Influence of Polarization Functions on Molecular Orbital Hydrogenation Energies. *Theoretica chimica acta* **1973**, *28*, 213-222.

82. Hehre, W. J.; Ditchfield, R.; Pople, J. A., Self—Consistent Molecular Orbital Methods. Xii. Further Extensions of Gaussian—Type Basis Sets for Use in Molecular Orbital Studies of Organic Molecules. *The Journal of Chemical Physics* **1972**, *56*, 2257-2261.

83. Kratz, E. G.; Duke, R. E.; Cisneros, G. A., Long-Range Electrostatic Corrections in Multipolar/Polarizable Qm/Mm Simulations. *Theor Chem Acc* **2016**, *135*, 1-9.

84. Parks, J. M.; Hu, H.; Cohen, A. J.; Yang, W., A Pseudobond Parametrization for Improved Electrostatics in Quantum Mechanical/Molecular Mechanical Simulations of Enzymes. *The Journal of chemical physics* **2008**, *129*.

85. Fang, D.; Chaudret, R.; Piquemal, J. P.; Cisneros, G. A., Toward a Deeper Understanding of Enzyme Reactions Using the Coupled Elf/Nci Analysis: Application to DNA Repair Enzymes. *J Chem Theory Comput* **2013**, *9*, 2156-60.

86. Johnson, E. R.; Keinan, S.; Mori-Sanchez, P.; Contreras-Garcia, J.; Cohen, A. J.; Yang, W., Revealing Noncovalent Interactions. *J Am Chem Soc* **2010**, *132*, 6498-506.

87. Lu, T.; Chen, F., Multiwfn: A Multifunctional Wavefunction Analyzer. *J Comput Chem* **2012**, *33*, 580-92.

88. Becke, A. D.; Edgecombe, K. E., A Simple Measure of Electron Localization in Atomic and Molecular-Systems. *J Chem Phys* **1990**, *92*, 5397-5403.

89. Yang, S.; Xu, G. Y.; Han, J. P.; Bing, H.; Dou, H.; Zhang, X. G., Nitrogen-Doped Porous Carbon Derived from Dopamine-Modified Polypyrrole and Its Electrochemical Capacitive Behavior. *Acta Phys-Chim Sin* **2015**, *31*, 685-692.

90. Lu, T.; Chen, F. W., Meaning and Functional Form of the Electron Localization Function. *Acta Phys-Chim Sin* **2011**, *27*, 2786-2792.

91. Dennington, R.; Keith, T. A.; Millam, J. M., Gaussview 6.1.1. *Semichem Inc.: Shawnee Mission, KS* **2019**.

92. Naseem-Khan, S.; Berger, M. B.; Leddin, E. M.; Maghsoud, Y.; Cisneros, G. A., Impact of Remdesivir Incorporation Along the Primer Strand on Sars-Cov-2 Rna-Dependent Rna Polymerase. *Journal of Chemical Information and Modeling* **2022**, *62*, 2456-2465.

93. Maghsoud, Y.; Dong, C.; Cisneros, G. A., Investigation of the Inhibition Mechanism of Xanthine Oxidoreductase by Oxipurinol: A Computational Study. *Journal of Chemical Information and Modeling* **2023**.

94. Maghsoud, Y.; Dong, C.; Cisneros, G. A., Computational Characterization of the Inhibition Mechanism of Xanthine Oxidoreductase by Topiroxostat. *ACS Catalysis* **2023**, *13*, 6023-6043.

95. Maghsoud, Y.; Jayasinghe-Arachchige, V. M.; Kumari, P.; Cisneros, G. A.; Liu, J., Leveraging Qm/Mm and Molecular Dynamics Simulations to Decipher the Reaction Mechanism of the Cas9 Hnh Domain to Investigate Off-Target Effects. *Journal of Chemical Information and Modeling* **2023**, *63*, 6834-6850.

96. Mills, K.; Misra, J.; Torabifard, H., Allosteric Modulation of Yap/Taz-Tead Interaction by Palmitoylation and Small Molecule Inhibitors. *bioRxiv* **2023**, 2023.10. 24.563887.

97. Leddin, E. M.; Group, C. R.; Cisneros, G. A. *Cisnerosresearch/Amber-Eda: Updated Stddev Calculation*, v1.0; 2021.

98. Team, R. C., In; 2021.

99. Freudenthal, B. D.; Beard, W. A.; Perera, L.; Shock, D. D.; Kim, T.; Schlick, T.; Wilson, S. H., Uncovering the Polymerase-Induced Cytotoxicity of an Oxidized Nucleotide. *Nature* **2015**, *517*, 635-639.

100. Jamsen, J. A.; Beard, W. A.; Pedersen, L. C.; Shock, D. D.; Moon, A. F.; Krahn, J. M.; Bebenek, K.; Kunkel, T. A.; Wilson, S. H., Time-Lapse Crystallography Snapshots of a Double-Strand Break Repair Polymerase in Action. *Nature Communications* **2017**, *8*, 253.

101. Reed, A. J.; Suo, Z., Time-Dependent Extension from an 8-Oxoguanine Lesion by Human DNA Polymerase Beta. *Journal of the American Chemical Society* **2017**, *139*, 9684-9690.

102. Nakamura, T.; Zhao, Y.; Yamagata, Y.; Hua, Y.-j.; Yang, W., Watching DNA Polymerase H Make a Phosphodiester Bond. *Nature* **2012**, *487*, 196-201.

103. Vyas, R.; Reed, A. J.; Tokarsky, E. J.; Suo, Z., Viewing Human DNA Polymerase B Faithfully and Unfaithfully Bypass an Oxidative Lesion by Time-Dependent Crystallography. *Journal of the American Chemical Society* **2015**, *137*, 5225-5230.

104. Sucato, C. A.; Upton, T. G.; Kashemirov, B. A.; Osuna, J.; Oertell, K.; Beard, W. A.; Wilson, S. H.; Florián, J.; Warshel, A.; McKenna, C. E., DNA Polymerase B Fidelity: Halomethylene-Modified Leaving Groups in Pre-Steady-State Kinetic Analysis Reveal Differences at the Chemical Transition State. *Biochemistry* **2008**, *47*, 870-879.

105. Wang, L.; Yu, X.; Hu, P.; Broyde, S.; Zhang, Y., A Water-Mediated and Substrate-Assisted Catalytic Mechanism for Sulfolobus Solfataricus DNA Polymerase Iv. *Journal of the American Chemical Society* **2007**, *129*, 4731-4737.

106. Wang, Y.; Schlick, T., Quantum Mechanics/Molecular Mechanics Investigation of the Chemical Reaction in Dpo4 Reveals Water-Dependent Pathways and Requirements for Active Site Reorganization. *Journal of the American Chemical Society* **2008**, *130*, 13240-13250.

107. Wang, L.; Broyde, S.; Zhang, Y., Polymerase-Tailored Variations in the Water-Mediated and Substrate-Assisted Mechanism for Nucleotidyl Transfer: Insights from a Study of T7 DNA Polymerase. *Journal of molecular biology* **2009**, *389*, 787-796.

108. Lior-Hoffmann, L.; Ding, S.; Geacintov, N. E.; Zhang, Y.; Broyde, S., Structural and Dynamic Characterization of Polymerase K's Minor Groove Lesion Processing Reveals How Adduct Topology Impacts Fidelity. *Biochemistry* **2014**, *53*, 5683-5691.

109. Fang, D.; Chaudret, R.; Piquemal, J.-P.; Cisneros, G. A. s., Toward a Deeper Understanding of Enzyme Reactions Using the Coupled Elf/Nci Analysis: Application to DNA Repair Enzymes. *Journal of Chemical Theory and Computation* **2013**, *9*, 2156-2160.

110. Cisneros, G. A.; Perera, L.; García-Díaz, M.; Bebenek, K.; Kunkel, T. A.; Pedersen, L. G., Catalytic Mechanism of Human DNA Polymerase Λ with Mg2+ and Mn2+ from Ab Initio Quantum Mechanical/Molecular Mechanical Studies. *DNA repair* **2008**, *7*, 1824-1834.

111. Alberts, I. L.; Wang, Y.; Schlick, T., DNA Polymerase B Catalysis: Are Different Mechanisms Possible? *Journal of the American Chemical Society* **2007**, *129*, 11100-11110.

112. Genna, V.; Vidossich, P.; Ippoliti, E.; Carloni, P.; De Vivo, M., A Self-Activated Mechanism for Nucleic Acid Polymerization Catalyzed by DNA/Rna Polymerases. *Journal of the American Chemical Society* **2016**, *138*, 14592-14598.

113. Bojin, M. D.; Schlick, T., A Quantum Mechanical Investigation of Possible Mechanisms for the Nucleotidyl Transfer Reaction Catalyzed by DNA Polymerase B. *The Journal of Physical Chemistry B* **2007**, *111*, 11244-11252.

114. Lin, P.; Pedersen, L. C.; Batra, V. K.; Beard, W. A.; Wilson, S. H.; Pedersen, L. G., Energy Analysis of Chemistry for Correct Insertion by DNA Polymerase B. *Proceedings of the National Academy of Sciences* **2006**, *103*, 13294-13299.

115. Perera, L.; Freudenthal, B. D.; Beard, W. A.; Pedersen, L. G.; Wilson, S. H., Revealing the Role of the Product Metal in DNA Polymerase B Catalysis. *Nucleic Acids Research* **2017**, *45*, 2736-2745.

116. Gao, Y.; Yang, W., Capture of a Third Mg2+ Is Essential for Catalyzing DNA Synthesis. *Science* **2016**, *352*, 1334-1337.

117. Beard, W. A.; Wilson, S. H., Structure and Mechanism of DNA Polymerase B. *Biochemistry* **2014**, *53*, 2768-2780.

118. Freudenthal, B. D.; Beard, W. A.; Shock, D. D.; Wilson, S. H., Observing a DNA Polymerase Choose Right from Wrong. *Cell* **2013**, *154*, 157-168.

119. Stevens, D. R.; Hammes-Schiffer, S., Exploring the Role of the Third Active Site Metal Ion in DNA Polymerase H with Qm/Mm Free Energy Simulations. *Journal of the American Chemical Society* **2018**, *140*, 8965-8969.

120. Roston, D.; Demapan, D.; Cui, Q., Extensive Free-Energy Simulations Identify Water as the Base in Nucleotide Addition by DNA Polymerase. *Proceedings of the National Academy of Sciences* **2019**, *116*, 25048-25056.

121. Perera, L.; Freudenthal, B. D.; Beard, W. A.; Shock, D. D.; Pedersen, L. G.; Wilson, S. H., Requirement for Transient Metal Ions Revealed through Computational Analysis for DNA Polymerase Going in Reverse. *Proceedings of the National Academy of Sciences* **2015**, *112*, E5228-E5236.

122. Yang, W.; Weng, P. J.; Gao, Y., A New Paradigm of DNA Synthesis: Three-Metal-Ion Catalysis. *Cell & bioscience* **2016**, *6*, 1-7.

123. Nakamura, T.; Zhao, Y.; Yamagata, Y.; Hua, Y.-j.; Yang, W., Mechanism of the Nucleotidyl-Transfer Reaction in DNA Polymerase Revealed by Time-Resolved Protein Crystallography. *Biophysics* **2013**, *9*, 31-36.

124. Sassa, A.; Niimi, N.; Fujimoto, H.; Katafuchi, A.; Grúz, P.; Yasui, M.; Gupta, R. C.; Johnson, F.; Ohta, T.; Nohmi, T., Phenylalanine 171 Is a Molecular Brake for Translesion Synthesis across Benzo [a] Pyrene-Guanine Adducts by Human DNA Polymerase Kappa. *Mutation Research/Genetic Toxicology and Environmental Mutagenesis* **2011**, *718*, 10-17.

125. Choi, J.-Y.; Lim, S.; Kim, E.-J.; Jo, A.; Guengerich, F. P., Translesion Synthesis across Abasic Lesions by Human B-Family and Y-Family DNA Polymerases A, Δ, H, I, K, and Rev1. *Journal of molecular biology* **2010**, *404*, 34-44.

126. Perlow, R. A.; Broyde, S., Toward Understanding the Mutagenicity of an Environmental Carcinogen: Structural Insights into Nucleotide Incorporation Preferences. *Journal of molecular biology* **2002**, *322*, 291-309.

127. Batra, V. K.; Perera, L.; Lin, P.; Shock, D. D.; Beard, W. A.; Pedersen, L. C.; Pedersen, L. G.; Wilson, S. H., Amino Acid Substitution in the Active Site of DNA Polymerase B Explains the Energy Barrier of the Nucleotidyl Transfer Reaction. *Journal of the American Chemical Society* **2013**, *135*, 8078-8088.

128. Cavanaugh, N. A.; Beard, W. A.; Batra, V. K.; Perera, L.; Pedersen, L. G.; Wilson, S. H., Molecular Insights into DNA Polymerase Deterrents for Ribonucleotide Insertion*♦. *Journal of Biological Chemistry* **2011**, *286*, 31650-31660.

129. Garcia-Diaz, M.; Bebenek, K.; Larrea, A. A.; Havener, J. M.; Perera, L.; Krahn, J. M.; Pedersen, L. C.; Ramsden, D. A.; Kunkel, T. A., Template Strand Scrunching During DNA Gap Repair Synthesis by Human Polymerase Λ. *Nature structural & molecular biology* **2009**, *16*, 967-972.

130. Rungrotmongkol, T.; Mulholland, A. J.; Hannongbua, S., Active Site Dynamics and Combined Quantum Mechanics/Molecular Mechanics (Qm/Mm) Modelling of a Hiv-1 Reverse Transcriptase/DNA/Dttp Complex. *Journal of molecular graphics and modelling* **2007**, *26*, 1-13.

131. Castro, C.; Smidansky, E.; Maksimchuk, K. R.; Arnold, J. J.; Korneeva, V. S.; Götte, M.; Konigsberg, W.; Cameron, C. E., Two Proton Transfers in the Transition State for Nucleotidyl Transfer Catalyzed by Rna-and DNA-Dependent Rna and DNA Polymerases. *Proceedings of the National Academy of Sciences* **2007**, *104*, 4267-4272.

132. Castro, C.; Smidansky, E. D.; Arnold, J. J.; Maksimchuk, K. R.; Moustafa, I.; Uchida, A.; Götte, M.; Konigsberg, W.; Cameron, C. E., Nucleic Acid Polymerases Use a General Acid for Nucleotidyl Transfer. *Nature structural & molecular biology* **2009**, *16*, 212-218.